https://doi.org/10.5194/acp-2022-25
Preprint. Discussion started: 17 March 2022
© Author(s) 2022. CC BY 4.0 License.

Atmospheric Chemistry and Physics Discussions

MAX-DOAS observations of formaldehyde and nitrogen dioxide at three sites in Asia and comparison with the global chemistry transport model CHASER

Hossain Mohamed Syedul Hoque[1], Kengo Sudo[1,2], Hitoshi Irie[3], Alessandro Damiani[3], Manish Naja[4], and Al Mashroor Fatmi[3]

[1]Graduate School of Environmental Studies, Nagoya University, Nagoya, 4640064, Japan
[2]Japan Agency for Marine-Earth Science and Technology (JAMSTEC), Kanagawa, 2370061, Japan
[3]Center for Environmental Remote Sensing (CEReS), Chiba University, Chiba,2638522, Japan
[4]Aryabhatta Research Institute for Observational Sciences (ARIES), Manora Peak, Nainital-263001, Uttarakhand, India

Correspondence to: Hossain Mohammed Syedul Hoque (hoque.hossain.mohammed.syedul.u6@f.mail.nagoya-u.ac.jp)

Abstract. Formaldehyde (HCHO) and nitrogen dioxide (NO_2) concentrations and profiles were retrieved from ground-based multi-axis differential optical absorption spectroscopy (MAX-DOAS) observations during January 2017 through December 2018 at three sites in Asia: (1) Phimai (15.18°N, 102.5°E), Thailand; (2) Pantnagar (29°N, 78.90°E) in the Indo Gangetic plain (IGP), India; and (3) Chiba (35.62°N, 140.10°E), Japan. The observations were used to evaluate the NO_2 and HCHO partial columns and profiles (0-4 km) simulated using the global chemistry transport model (CTM) CHASER. The NO_2 and HCHO concentrations at all three sites showed consistent seasonal variations throughout the investigated period. Biomass burning affected the HCHO and NO_2 variation in Phimai during the dry season and in Pantnagar during spring (March-May) and post-monsoon (September-November). The results on the HCHO to NO_2 ratio (R_{FN}), an indicator of high ozone sensitivity, show that the transition region (i.e., $1< R_{FN} <2$) changes regionally, echoing the recent finding on the effectiveness of R_{FN}. Moreover, reasonable estimates of transition regions can be derived accounting for the NO_2- HCHO chemical feedback.

https://doi.org/10.5194/acp-2022-25
Preprint. Discussion started: 17 March 2022
© Author(s) 2022. CC BY 4.0 License.

Atmospheric Chemistry and Physics Discussions

CHASER demonstrated good performances reproducing the HCHO and NO_2 abundances at Phimai, mainly above 500 m from the surface. Model results agree with the measured variations, ranging within the one sigma standard deviation of the observations. Despite the complex terrain of Pantnagar (mountainous terrain), the modeled NO_2 estimates between 1.8 – 2km were reasonable. Simulations at higher resolution improved the modeled NO_2 estimates in Chiba, reducing the mean bias error (MBE) in the 0-2 km height by 35%. However, resolution-based improvements were limited to the surface layers. Sensitivity studies showed pyrogenic emissions in Phimai contribute to the HCHO and NO_2 concentrations up to ~ 50 and ~35%, respectively.

1 Introduction

Formaldehyde (HCHO) is the most abundant carbonyl compound in the atmosphere. It is a high-yield product of oxidization of all primary volatile organic compounds (VOCs) emitted from natural and anthropogenic sources by hydroxyl radicals (OH). Oxidation of long-lived VOCs such as methane produces a global HCHO background concentration of 0.2–1.0 ppbv in remote marine environments (Weller et al., 2000; Burkert et al., 2001; Singh et al., 2004; Sinreich et al., 2005). Aside from oxidation of VOCs, the significant sources of HCHO are direct emission from biomass burning, industrial processes, fossil fuel combustion (Lee et al., 1997; Hak et al., 2005; Fu et al., 2008;), and vegetation (Seco et al., 2007). However, oxidization of non-methane VOCs emitted from biogenic (e.g., isoprene) or anthropogenic (e.g., butene) sources govern the spatial variability of HCHO on a global scale (Franco et al., 2015). The sinks of HCHO include photolysis at wavelengths below 400 nm, oxidation by OH, and wet deposition, thereby limiting the lifetime to a few hours (Arlander et al., 1995).

Nitrogen dioxide (NO_2) is an important atmospheric constituent that (1) participates in the catalytic formation of tropospheric ozone (O_3), (2) acts as a catalyst for stratospheric ozone (O_3) destruction (Crutzen, 1970), (3) contributes to the formation of aerosols (Jang and Kamens, 2001), (4) acts as a precursor of acid rain (Seinfeld and Pandis, 1998), and (5) strongly affects radiative forcing (Lelieved et al., 2002; Solomon et al. 1999). Nitrogen oxides (NO_x = NO (nitric oxide) + NO_2) are emitted from natural and anthropogenic sources. Primary NO_x emission sources are biomass burning, fossil fuel combustion, soil emissions, and lightning (Bond et al., 2001; Zhang et al., 2003). NO_x emissions degrade air quality and are a leading air pollutant with global and national ambient air quality standards (Ma et al., 2013).

https://doi.org/10.5194/acp-2022-25
Preprint. Discussion started: 17 March 2022
© Author(s) 2022. CC BY 4.0 License.

Atmospheric Chemistry and Physics Discussions

Both HCHO and NO_2 are important intermediates in the global VOC–HO_x (hydrogen oxides)–NO_x catalytic cycle, which governs the O_3 chemistry in the troposphere (Lee et al., 1997; Houweling et al., 1998; Kanakidou et al., 2005; Hak et al., 2005). Thus, both trace gases play crucial roles in tropospheric chemistry.

The working principle of multi-axis differential optical absorption spectroscopy (MAX-DOAS), a well-established remote sensing method for measuring trace gases and aerosols, is based on the DOAS technique. Aerosols and trace gases are quantified using selective narrowband (high frequency) absorption features (Platt 1994, Platt and Stutz 2008). Spectral radiation measurements at different elevation angles (ELs) can provide profile information of atmospheric trace gases and aerosols (Hönninger et al., 2004; Wagner et al., 2004; Wittrock et al., 2004; Frieß et al., 2006; Irie et al., 2008a). Many studies have demonstrated the retrieval of aerosol and trace gas concentrations and profiles from MAX-DOAS observations, including NO_2 and HCHO (Clémer et al., 2010; Irie et al., 2011; Hendrick et al., 2014; Franco et al., 2015; Frieß et al., 2016; Wang et al., 2014).

The ability of MAX-DOAS to provide information related to surface concentrations, vertical profiles, and column densities makes it complementary to ground-based in situ and satellite observations. Moreover, the MAX-DOAS method uses narrowband absorption of the target compounds, thereby obviating the radiometric calibration of the instrument. Because of these advantages, MAX-DOAS systems are deployed for the assessment of aerosol and trace gases in regional and global observational networks such as BREDOM (Wittrock et al., 2004), BIRA-IASB (Clémer et al., 2010), and MADRAS (Kanaya et al., 2014). Such datasets are used in but are not limited to (1) air quality assessment and monitoring, (2) evaluation of chemistry-transport models (CTMS), and (3) validation of satellite retrieval. Several studies have used MAX-DOAS datasets to validate tropospheric columns retrieved from satellite observations, including NO_2 and HCHO (Ma et al., 2013; Irie et al., 2008b; Chan et al., 2020; Ryan et al., 2020). However, limited MAX-DOAS datasets have been used to evaluate global CTMs. Vigouroux et al. (2009) and Franco et al. (2015) respectively used the MAX-DOAS HCHO datasets from Reunion Island and Jungfraujoch stations to evaluate the IMAGES (Intermediate Model of Annual and Global Evolution of Species) and GEOS-Chem model simulations. Kanaya et al. (2014) validated the MIROC-

https://doi.org/10.5194/acp-2022-25
Preprint. Discussion started: 17 March 2022
© Author(s) 2022. CC BY 4.0 License.

Atmospheric Chemistry and Physics Discussions

ESM-CHEM (Model for Interdisciplinary Research on Climate–Earth System Model – Chemistry) simulated NO_2 column densities with MAX-DOAS observations in Cape Hedo and Fukue in Japan. Kumar et al. (2021) utilized MAX-DOAS observations to evaluate the high-resolution regional model Meco(n)(MESSy-field ECHAM and COSMO model nested n times).

In this study, NO_2 and HCHO profiles retrieved from MAX-DOAS observations at the A-SKY (International air quality and sky research remote sensing) (http://atmos3.cr.chiba-u.jp/a-sky/) network sites are utilized to evaluate the global Chemical Atmospheric General Circulation Model for the Study of Atmospheric Environment and Radiative Forcing (CTM CHASER; Sudo et al., 2002). The three A-SKY sites - (1) Phimai in Thailand (15.18°N, 102.56°E), (2) Pantnagar (29°N, 78.90°E) in the Indo Gangetic plain (IGP) in India, and (3) Chiba (35.62°N, 140.10°E) in Japan, are representative of rural, semi-rural, and urban environments, respectively. CHASER has been used mostly for global-scale research (Sudo et al., 2007; Sekiya et al., 2014, 2018; Miyazaki et al., 2017). This report is the first attempt to evaluate the CHASER-simulated NO_2 and HCHO profiles using MAX-DOAS observations in three atmospheric environments. Moreover, limited literature has described the use of MAX-DOAS datasets to evaluate global CTMs in the south and southeast Asian regions. Overall, this study was conducted to provide important insights into the model performances and help reduce model uncertainties related to NO_2 and HCHO simulations in these regions.

The manuscript is structured in the following manner. First, the observation sites, MAX-DOAS instrumentation, and retrieval strategies are described in section 2. Section 2 also includes a short description of the CHASER model. Next, the observations and the evaluation of the model are presented in sections 3.1 and 3.2, respectively. Finally, the sensitivity study results are provided in section 3.3. and the concluding remarks in section 4.

https://doi.org/10.5194/acp-2022-25
Preprint. Discussion started: 17 March 2022
© Author(s) 2022. CC BY 4.0 License.

Atmospheric Chemistry and Physics Discussions

2 Observations, datasets, and methods

2.1 Site Information

Continuous MAX-DOAS observations at Phimai, Pantnagar, and Chiba started in 2014, 2017, and 2012, respectively. The measurements from January 2017 to December 2018 at all three sites are discussed here. Phimai, a rural site, is located ~260 km northeast of the Bangkok metropolitan region and is unlikely to be affected by vehicular and industrial emissions. However, the site is affected by biomass burning from January to April. Two major air streams: the dry, cool northeast monsoon during November – mid-February and the wet, warm southwest monsoon during mid-May – September affect the climate in Phimai. Following Hoque et al. (2018), the climate classification of Phimai is : (a) dry season (January – April), and (b) wet season (June – September).

Pantnagar, a semi-urban site in India, is located in the Indo-Gangetic Plain region (IGP). The Indian capital of New Delhi is situated at ~225 km southwest of the site. The low-altitude plains are on the south and west side of the site, whereas the Himalayan mountains are located to the north and east. An important roadway with moderate traffic volume and a small local airport lies within 3 km of the site. Rudrapur (~12 km southwest of Pantnagar) and Haldwani (~ 25 km northeast of Pantnagar) are the two major cities near Pantnagar, having a few small-scale industries. Climate classification in Pantnagar is the following: (1) winter (December–February), (2) spring (March-May), (3) summer monsoon (June–August), and (4) autumn (September–November).

Chiba, an urban site, is located ~40 km southeast of the Tokyo metropolitan region. Tokyo Bay, large-scale industries, and residential areas are located within a 50 km radius. The climate in Chiba is divided into four seasons: (1) spring (March-May), (2) summer (June–August), (3) autumn (September–November), and winter (December– February). The locations of the three sites are depicted in Fig. 1.

https://doi.org/10.5194/acp-2022-25
Preprint. Discussion started: 17 March 2022
© Author(s) 2022. CC BY 4.0 License.

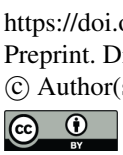

Atmospheric Chemistry and Physics Discussions

136

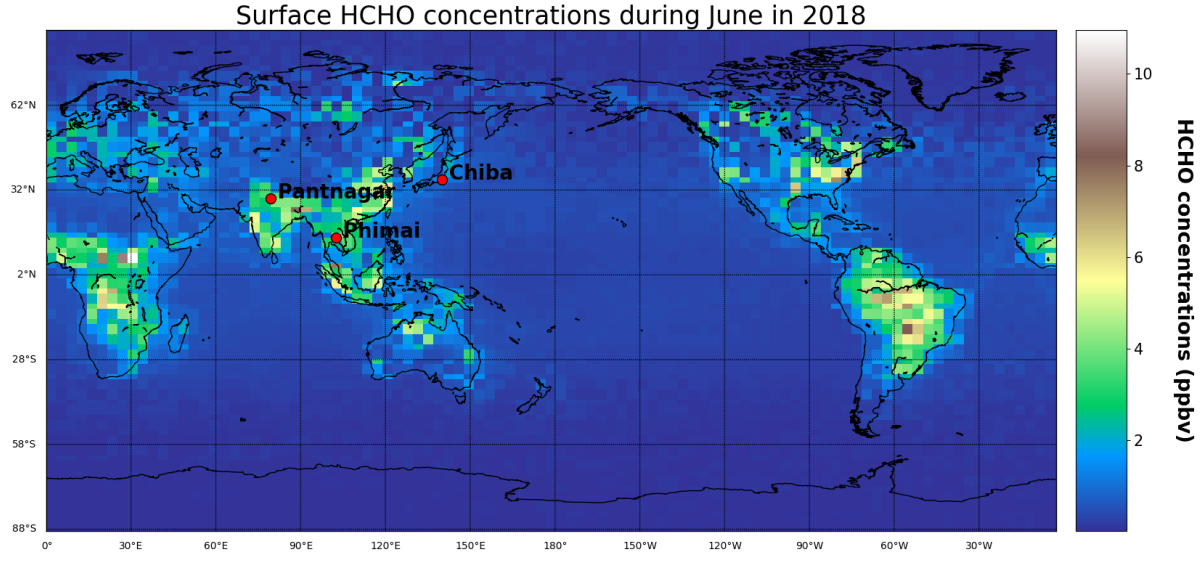

137 **Figure 1:** Surface HCHO concentrations during June 2018, simulated using the CHASER model. The
138 red points indicate the locations of the observation sites, which are part of the A-SKY network.

139

140

141 2.2 MAX-DOAS retrieval

142 The MAX-DOAS systems used for continuous observations at the three sites participated in the Cabauw
143 Intercomparison Campaign of Nitrogen Dioxide measuring Instruments (CINDI) (Roscoe et al., 2010)
144 and CINDI-2 (Kreher et al., 2020) campaign. The instrumentation setup is described by Irie et al. (2008,
145 2011, 2015). The indoor part of the MAX-DOAS systems consists of an ultraviolet-visible (UV-VIS)
146 spectrometer (Maya2000Pro; Ocean Optics Inc.) embedded in a temperature-controlled box. The outdoor
147 unit consist of a single telescope and a 45° inclined movable mirror on a rotary actuator, used to perform
148 reference and off-axis measurements. The high-resolution spectra from 310–515 nm is recorded at six

https://doi.org/10.5194/acp-2022-25
Preprint. Discussion started: 17 March 2022
© Author(s) 2022. CC BY 4.0 License.

Atmospheric Chemistry and Physics Discussions

elevation angles (ELs) of 2°, 3°, 4°, 6°, 8°, and 70° at the Chiba and Phimai sites. At the Pantnagar site, measurements are conducted at ELs of 3°, 4°, 5°, 6°, 8°, and 70°. The sequences of the ELs at all the sites were repeated every 15 min. The reference spectra is recorded at EL of 70° instead of 90° to minimize variations in the measured signals. The off-axis ELs is limited to < 10° to reduce the systematic error in the in-oxygen collision complex (O_4) fitting results (Irie et al., 2015), thereby maintaining high sensitivity in the lowest layer of the retrieved aerosol and trace gas profiles. Daily wavelength calibration using the high-resolution solar spectrum from Kurucz et al. (1984) is performed to account for the spectrometer's long-term degradation. The spectral resolution (full width half maximum: FWHM) is about 0.4 nm at 357 and 476 nm. The concentrations and profiles of aerosol and trace gases are retrieved using the Japanese vertical profile retrieval algorithm (JM2 ver. 2) (Irie et al., 2011, 2015). The algorithm works in three steps: (1) DOAS fittings, (2) profile/column retrieval of aerosol, and (3) profile/column retrieval of trace gases. Irie et al. (2008a, 2008b, 2011, 2015) described the retrieval procedures, and the error estimates. Here we provide a short overview.

First, the differential slant column density (ΔSCD) of trace gases is retrieved using the DOAS technique (Platt 1994), which uses the nonlinear least-squares spectral fitting method, according to the following equation.

$$lnI(\lambda) = ln(I_o(\lambda) - c(\lambda)) - \sum_{i}^{n} \sigma_i(\lambda)\Delta SCD_i - p(\lambda) \quad (1)$$

Therein, $I_o(\lambda)$ represents the reference spectrum measured at time *t*. $I_o(\lambda)$ is derived by interpolating two reference spectra (i.e., EL=70°) within 15 min before and after the complete sequential scan of the off-axis ELs at time *t*. ΔSCD represents the difference between the slant column density along the off-axis and reference spectrum. Second- and third-order polynomials are fitted to account for the wavelength-dependent offset $c(\lambda)$ and the effect of molecular and particle scattering $p(\lambda)$, respectively. Also, $c(\lambda)$ accounts for the influence of stray light. The HCHO ΔSCD and NO_2 ΔSCD are retrieved from the fitting windows of 336–359 and 460–490 nm, respectively. Significant O_4 absorptions in the 338–370 and 460–490 nm fitting windows are utilized to retrieve the O_4 ΔSCDs. The absorption cross-section

https://doi.org/10.5194/acp-2022-25
Preprint. Discussion started: 17 March 2022
© Author(s) 2022. CC BY 4.0 License.

Atmospheric Chemistry and Physics Discussions

175 data and the fitted absorbers in the HCHO and NO_2 fitting windows are given in table 1. Figure 2 presents
176 an example of the fitting results.

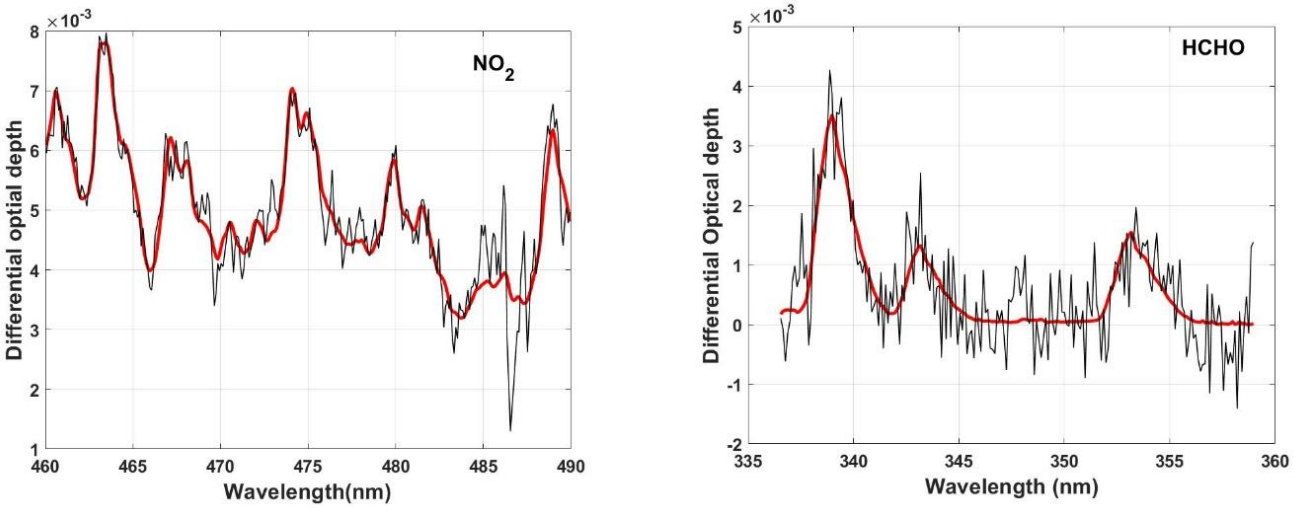

177 **Figure 2:** Examples of spectral fitting of NO_2 and HCHO, where the red and black lines show the scaled cross-
178 section and the summation of scaled cross-sections and fitting residuals, respectively. The example is shown for
179 the measurements on 10 April 2017, in Phimai at 10:00 LT at an EL of 2°.

180 In the second step, the aerosol optical depth (AOD) τ and the vertical profiles of the aerosol extinction
181 coefficient (AEC) k are retrieved using the optimal estimation method (Irie et al., 2008a; Rogers, 2000)
182 The measurement vector y (representing the quantities to be fitted) and state vector (representing the
183 retrieved quantities) is defined as

184

185 $$y = (O_4 \Delta SCD(\Omega_1) \dots\dots\dots \Delta SCD(\Omega_n))^T \quad (2) \text{ and}$$

186 $$x = (\tau F_1 F_2 F_3)^T \quad (3),$$

https://doi.org/10.5194/acp-2022-25
Preprint. Discussion started: 17 March 2022
© Author(s) 2022. CC BY 4.0 License.

Atmospheric Chemistry and Physics Discussions

187

188 **Table 1.** Cross section data references and absorbers fitted in the HCHO and NO_2 window

Cross-section	Absorbers fitted	Data Source
O_3		*Bougmil et al.* [2003], 223K
NO_2	O_3, NO_2, H_2O, O_4, Ring	*Vandaele et al.* [1996], 295K
BrO		*Fleischmann et al.* [2004], 223K
Ring		*Chance and Spurr* [1997]
H_2O		*Vandaele et al.* [2005], 280K
O_4		Hermans et al. [2003], 296K
HCHO	O_3, NO_2, HCHO, BrO, O_4, Ring	*Meller and Moortgart* [2000], 293k

189

190

191 where *n* stands for the number of measurements within one complete scan of an EL sequence. Ω denotes
192 the viewing geometry and compromise three components: solar zenith angle (SZA), EL, and relative
193 azimuth angle (RAA). The *F* values determine the profile shape, with values between 0 and 1. The partial
194 AOD for 0–1, 1–2, 2–3, and above 3 km layers were defined respectively as AOD ·F_1, AOD ·(1-F_1) F_2,
195 and AOD · (1-F_1) (1-F_2) F_3, and AOD ·(1-F_1) (1-F_2) (1-F_3). The AEC profile from 3 to 100 km is derived
196 assuming a fixed value at 100 km and exponential AEC profile shape. Similarly, the AEC profiles at 2–
197 3, 1–2, and 0–1 km were derived. Such parameterization provides the advantage that the AEC profile can
198 be retrieved with only the apriori knowledge of the *F* (profile shape) values and little or no information
199 related to the absolute AEC values in the troposphere. Irie et al. (2008a) demonstrated that the relative

https://doi.org/10.5194/acp-2022-25
Preprint. Discussion started: 17 March 2022
© Author(s) 2022. CC BY 4.0 License.

Atmospheric Chemistry and Physics Discussions

variability of the profile shape, in terms of 1-km averages, is smaller than that of the absolute AEC values. However, the vertical resolution and the measurement sensitivity cannot be derived directly with such a parameterization (Irie et al., 2008a; 2009). The retrievals and simulations conducted by other groups for similar geometries (i.e., Frieß et al., 2006) are used to overcome such limitations. The apriori values used for this study were similar to those reported by Irie et al. (2011): AOD = 0.21 ± 3.0, F_1 = 0.60 ± 0.05, F_2 = 0.80 ± 0.03, and F_3 = 0.80 ± 0.03.

Then, a lookup table (LUT) of the box air mass factor (A_{box}) vertical profile is constructed using the radiative transfer model JACOSPAR (Irie et al., 2015), which is based on the Monte Carlo Atmospheric Radiative Transfer Simulator (MCARaTS) (Iwabuchi, 2006). Results obtained from JACOSPAR are validated in the study of Wagner et al. (2007). The optimal aerosol load and the A_{box} profiles are derived using the A_{box} LUT and the O_4 ΔSCD at all ELs.

In the third step, the A_{box} profiles, HCHO and NO_2 ΔSCDs, and the nonlinear iterative inversion method are used to retrieve the HCHO and NO_2 vertical column densities (VCDs) and profiles. Here the NO_2 retrieval is explained.

For trace gas retrieval, the measurement vector and state vector are defined as

$$y = (NO2\Delta SCD(\Omega_1) \dots \dots \dots NO2\Delta SCD(\Omega_n))^T \quad (4)$$ and

$$x = (VCDf_1f_2f_3)^T \quad (5)$$

VCD represents the vertical column density below 5 km; f values are the profile shape factor. Above the 5 km layer, fixed profiles are assumed. Similarly, to aerosol retrieval, the partial VCD for the 0–1, 1–2, 2–3, and 3–5 km is defined respectively as VCD ·f_1, VCD ·(1-f_1) f_2, VCD · (1-f_1) (1-f_2) f_3, and VCD ·(1-f_1) (1-f_2) (1-f_3). Finally, the partial VCD values are converted to the volume mixing ratio (VMR) using the U.S. standard atmosphere temperature and pressure data scaled to the respective surface measurements.

The calculated vertical profile is converted to NO_2 ΔSCDs using the A_{box} LUT constructed for aerosol retrieval. However, the trace gas wavelengths differed from the representative wavelengths of A_{box} LUT (357 and 476 nm). Therefore, the AOD at the trace gas wavelength is estimated, converting the retrieved

https://doi.org/10.5194/acp-2022-25
Preprint. Discussion started: 17 March 2022
© Author(s) 2022. CC BY 4.0 License.

Atmospheric Chemistry and Physics Discussions

AOD to the closer aerosol wavelength of 357 or 476 nm, assuming the Angstrom exponent value of 1.00. Then, the A_{box} profiles from the LUT corresponding to the recalculated AOD values are selected. The dependence of the A_{box} profiles on the concentration profiles is expected to be minimal because both HCHO and NO_2 are optically thin absorbers (Wagner et al., 2007; Irie et al., 2011). For every 15 min (time required for one complete scan of ELs), 20% (the mean ratio of the retrieved VCD to maximum ΔSCD) of the maximum trace gas ΔSCDs is used as a priori information for the VCD retrievals. The a priori error is set to 100% of the maximum trace gas ΔSCD. Figure 3 presents the mean averaging kernel of the HCHO and NO_2 retrievals during the dry season in Phimai. The area calculated from the averaging kernel is close to unity. Therefore, the retrieved VCD is independent of the a priori values.

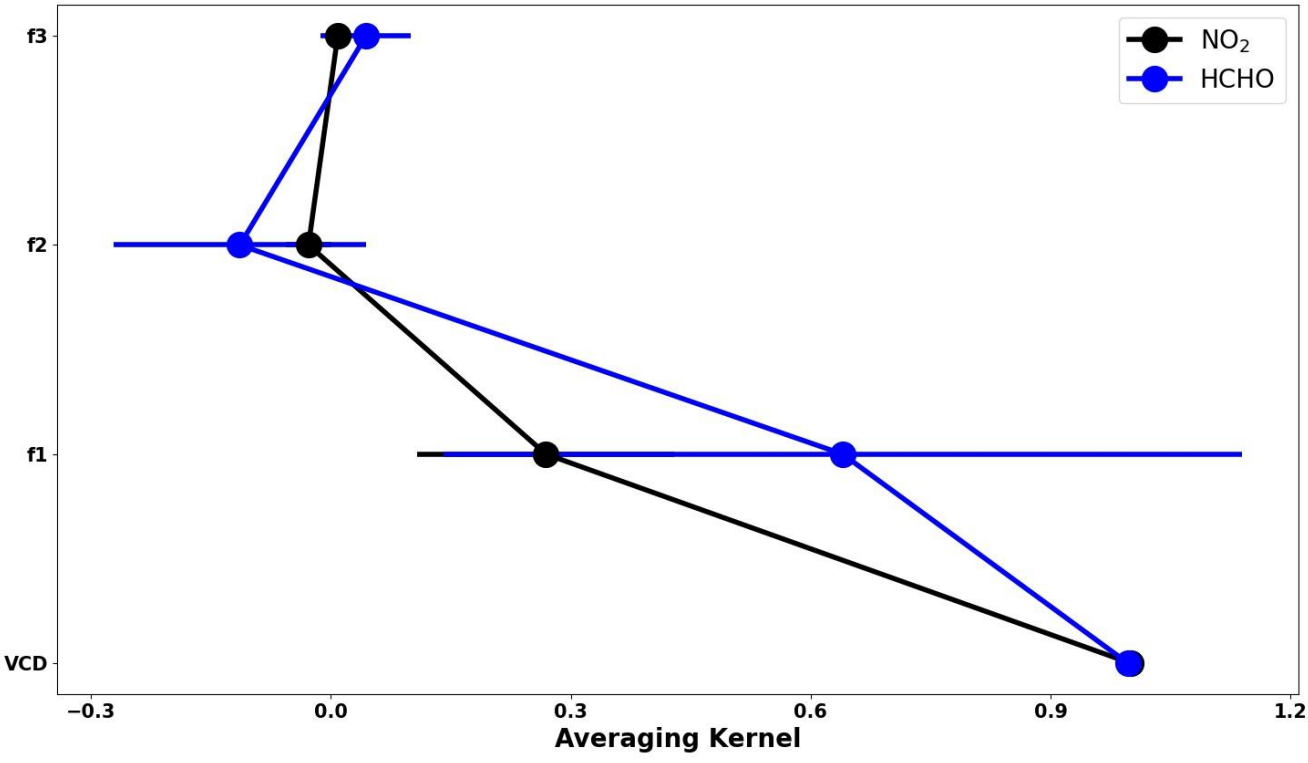

Figure 3: The mean averaging kernel of the NO_2 and HCHO retrievals from the observations in Phimai during 2017

https://doi.org/10.5194/acp-2022-25
Preprint. Discussion started: 17 March 2022
© Author(s) 2022. CC BY 4.0 License.

Atmospheric Chemistry and Physics Discussions

The total error of the retrieval consists of random and systematic errors. The measurement error covariance matrix constructed from the residuals of the respective trace gas ΔSCDs is used to estimate the random error. The systematic error is calculated assuming uncertainties as high as 30 and 50% in the retrieved AOD (or the corresponding A_{box} values). The total estimated error is shown in Table 2. Aside from the random and systematic error, more sources of error might exist. For instance, the bias in the ELs can induce uncertainties in the retrieved products. However, Hoque et al. (2018) demonstrated that such biases had a non-significant effect on the final retrieved products, mostly less than 5%.

The cloud screening procedure is similar to that described by Irie et al. (2011) and by Hoque et al. (2018a, 2018b). During the retrieval steps, retrieved AOD values greater than 3 are excluded. This is because optically thick clouds are primarily responsible for such large optical depth. Furthermore, filtering based on the residuals of O_4 and the trace gas ΔSCDs is also used to screen clouds. The screening criteria are: respective residuals of O_4, HCHO, and NO_2 ΔSCDs < 10%, < 50%, and <20%, and the degrees of freedom of the retrieval greater than 1.02.

Table 2. Estimated Errors (%) for the NO_2 and HCHO concentration in 0-1 km layer, retrieved using the JM2 algorithm

Retrieved Product	Random error	Systematic error	Error related to instrumentation	Total error
NO_2	10	12	5	16
HCHO	16	25	5	30

2.3 CHASER simulations

CHASER V4.0 (Sudo et al., 2002; Sudo and Akimoto, 2007; Sekiya and Sudo, 2014), coupled online with the MIROC-AGCM atmospheric general circulation model (AGCM) (K-1 model developers, 2004) and the SPRINTARS aerosol transport model (Takemura et al., 2005, 2009), is a global chemistry transport model to study the atmospheric environment and radiative forcing. In addition, several updates,

https://doi.org/10.5194/acp-2022-25
Preprint. Discussion started: 17 March 2022
© Author(s) 2022. CC BY 4.0 License.

Atmospheric Chemistry and Physics Discussions

including the introduction of aerosol species (sulfate, nitrate, etc.) and related chemistry, radiation, and cloud processes, have been implemented in the latest version of CHASER.

CHASER can calculate the concentrations of 92 species through 263 chemical reactions (gaseous, aqueous, and heterogeneous chemical reactions) considering the chemical cycle of O_3–HO_x – NO_x –CH_4–CO along with oxidation of non-methane volatile organic compounds (NMVOCs)(Miyazaki et al., 2017). CHASER simulates the stratospheric ozone chemistry considering the Chapman mechanisms, catalytic reactions related to halogen oxides (HO_x, NO_x, ClO_x, and BrO_x), and polar stratospheric clouds (PSCs). Resistance-based parameterization (Wesely, 1989), cumulus convection, and large-scale condensation parameterizations are used to calculate dry and wet depositions. The piecewise parabolic method (Colella

Table 3: The settings of the CHASER simulations used in the current study

Simulation	Anthropogenic emissions	Pyrogenic emissions	Biogenic emissions	Soil NO_x emission	Other physical and chemical processes
Standard	ON	ON	ON	ON	ON
L1_HCHO	ON	Pyrogenic VOCs switched	ON	ON	ON
L1_opt	ON	OFF	Reduced by 50%	ON	ON
L1_NO_2	ON	ON	ON	OFF	ON
L2		ON	ON	ON	ON

https://doi.org/10.5194/acp-2022-25
Preprint. Discussion started: 17 March 2022
© Author(s) 2022. CC BY 4.0 License.

Atmospheric Chemistry and Physics Discussions

	Anthropogenic VOC emissions switched OFF

and Woodward, 1984) and the flux-form semi-Lagrangian schemes (Lin and Rood, 1996) calculate advective tracer transport. CHASER simulates tracer transport on a sub-grid scale in the framework of the prognostic Arakawa–Schubert cumulus convection scheme (Emori et al., 2001) and the vertical diffusion scheme (Mellor and Yamada, 1974). In this study, CHASER simulations were conducted at a horizontal resolution of 2.8° × 2.8°, with 36 vertical layers from the surface to ~50 km altitude and a typical time step of 20 min. The meteorological fields simulated by MIROC-AGCM were nudged toward the six-hourly NCEP FNL reanalysis data at every model time step.

The anthropogenic, biomass burning, lightning, and soil emissions of NO_x were incorporated into CHASER simulations. Anthropogenic emissions were based on the HTAP_v2.2 for 2008. Biomass burning and soils emissions from the ECMWF/MAC reanalysis were used. The biogenic emissions for VOCs are based on the process-based biogeochemical model the Vegetation Integrative SImulator for Trace gases (VISIT) (Ito and Inatomi, 2012) simulations. The NO_x production from lightning is calculated based on the parameterization of Price and Rind (1992) linked to the convection scheme of the AGCM (Sudo et al., 2002). The isoprene, terpene, acetone, and ONMV emissions during July were 2.14×10^{-11}, 4.43×10^{-12}, 1.60×10^{-12}, and 9.93×10^{-13} $kgCm^{-2}s^{-1}$.

Multiple CHASER simulations with different settings used for this study are presented in Table 3.

https://doi.org/10.5194/acp-2022-25
Preprint. Discussion started: 17 March 2022
© Author(s) 2022. CC BY 4.0 License.

Atmospheric Chemistry and Physics Discussions

3 Results and discussion

3.1 Results from MAX-DOAS observations

3.1.1 HCHO seasonal variation

https://doi.org/10.5194/acp-2022-25
Preprint. Discussion started: 17 March 2022
© Author(s) 2022. CC BY 4.0 License.

Atmospheric Chemistry and Physics Discussions

306 The monthly mean HCHO concentrations in the 0–1 and 0–2 km layers from January 2017 – December
307 2018 and the corresponding one sigma (1σ) standard deviations for the three sites are depicted in Fig. 4.
308 The HCHO levels at the Phimai site show a consistent seasonal cycle, characterized by high
309 concentrations during the dry season. Such enhancement is related to the influence of biomass burning
310 during the dry season, which has been well documented in the work of Hoque et al. (2018). The HCHO
311 concentrations at Phimai peak in March or April, with a maximum of 4–6 ppbv. The variation in the peak
312 concentration and timing mainly depends on the intensity of biomass burning activities. During the wet
313 season, the HCHO concentrations are mostly within 2–3 ppbv, indicating a two-fold increase in the
314 HCHO abundances during the dry season. The daily mean HCHO amounts (0–1 km) are 0.78-9.84 ppbv,
315 representing seasonal modulation of 134%.

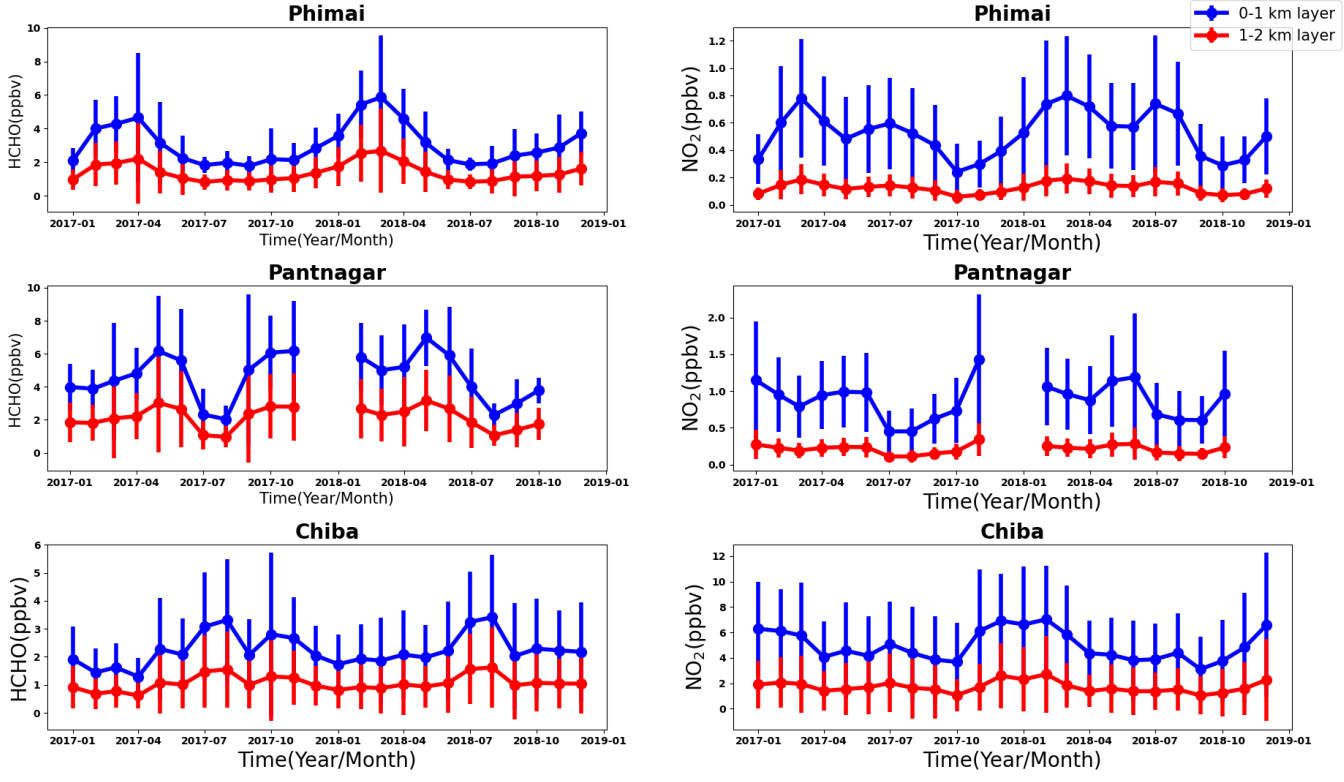

316

317 **Figure 4:** The seasonal variations in the HCHO (left panel) and NO_2 (right panel) concentrations in the 0-1 (blue)
318 and 1-2 (red) km layers in Phimai, Pantnagar, and Chiba. The error bars indicate the one sigma standard deviation

https://doi.org/10.5194/acp-2022-25
Preprint. Discussion started: 17 March 2022
© Author(s) 2022. CC BY 4.0 License.

Atmospheric Chemistry and Physics Discussions

of the mean values. The gaps in the plots for the Pantnagar site indicate the unavailability of observations during the investigated period.

The seasonal variation of HCHO in the 0–1 km layer at the Pantnagar site has been discussed by Hoque et al. (2018b). Here, the results are replotted to verify the consistency of the seasonal variations. Observations made during autumn in 2018 were not available because of problem with the spectrometer. Consistent seasonal variation of HCHO abundances is observed at the Pantnagar site, with enhanced concentrations during the spring. The Pantnagar site is affected by biomass burning during spring and autumn (Hoque et al., 2018b), explaining the high concentrations found during spring. In both years, the maximum HCHO concentrations are ~6 ppbv. The springtime peak occurs in May. The HCHO concentrations during the monsoon are ~35% lower than in the spring, indicating a strong effect of the monsoon on the HCHO concentrations found for Pantnagar. The seasonal modulation of HCHO at Pantnagar estimated from the daily mean concentrations is 107%. Under the influence of biomass burning, the maximum monthly HCHO concentrations are similar (~6 ppbv) at Phimai and Pantnagar. The maximum instantaneous concentrations of HCHO during biomass burning influence in Phimai and Pantnagar are 26 and 30 ppbv, respectively. Zarzana et al. (2017) reported HCHO abundances of ~60 ppbv in fresh biomass plumes in the US. The lower values obtained from our measurements might be attributable to (1) more aged plumes intercepted by the MAX-DOAS instruments and (2) differences in the types of biomass fuel used. A comparison of the literature values indicates that the retrieval of HCHO under biomass burning is reasonable.

Summertime maximum and wintertime minimum characterize the seasonal variations of HCHO at the Chiba site, with a peak at ~3 ppbv. The HCHO concentrations are ~2 ppbv during other seasons, similar to the HCHO concentrations in Phimai during the wet season. The seasonal variation amplitudes of HCHO in Chiba is ~94%. For a site with similar seasonal variation (i.e., summertime maximum and wintertime minimum), Franco et al. (2015) reported HCHO seasonal modulation of 88%.

The concentrations of HCHO in the 1–2 km layers at all three sites are lower, almost 50% the value of the concentrations in the 0–1 km layer. The HCHO seasonal variation amplitudes at Phimai, Pantnagar,

https://doi.org/10.5194/acp-2022-25
Preprint. Discussion started: 17 March 2022
© Author(s) 2022. CC BY 4.0 License.

Atmospheric Chemistry and Physics Discussions

and Chiba sites are, respectively, 131%, 102%, and 90% when calculated based on the HCHO concentration in the 1–2 km layers. The modulation further decreased when retrieved values for the 2–3 km layer R used.

3.1.2 NO_2 seasonal variation at the three sites

Figure 4 also shows the seasonal variation of NO_2 for 0–1 and 1–2 km layers at the three sites. The error bars represent the 1σ standard deviation of the mean values. The NO_2 seasonal variations at Phimai and Pantnagar sites are similar to those of HCHO. A pronounced peak attributable to biomass burning influence is observed during the dry season in Phimai (~0.8 ppbv) and spring (1.2 ppbv), and post-monsoon (1.4 ppbv) in Pantnagar. The lowest NO_2 concentrations in Phimai and Pantnagar are, respectively, ~0.2 and 0.5 ppbv. The NO_2 concentration in Chiba is higher (~7 ppbv) during winter. The longer lifetime of NO_x and lower NO/NO_2 ratio because of lower photochemical activity in winter results in high NO_2 concentrations in Chiba (Irie et al., 2021).

At Phimai, the NO_2 concentrations in both seasons are almost similar. However, when Hoque et al. (2018a) reported the seasonal variation of NO_2 at Phimai during 2015–2016, the NO_2 concentrations in the dry season were higher. Table 4 shows the number of fire events during the dry seasons from 2015 to 2018. The fire data are extracted from the MODIS Active Fire Detections database (https://firms.modaps.eosdis.nasa.gov, last accessed on 2021/12/15). Data fulfilling the following criteria are chosen – (a) data point located within 100 km of the Phimai site, (b) confidence of the data greater than 70%, and (c) observations during the daytime. The lower fire counts during 2017-2018 compared to 2015-2016 period coincide with the lower NO_2 concentrations in the former. Fire counts varied between 2017 and 2018 but did not impact the NO_2 levels. However, HCHO concentrations changed with the number of fire occurrences between 2015 – 2018 (i.e., Figure 1 and Hoque et al.,2018a).

At such low NO_2 levels in Phimai, soil NO_x emissions are likely to be a more relevant contribution to NO_2. Although NO_2 is not emitted directly from soils, biological processes emit NO, which rapidly converts to NO_2 (Hall et al., 1996). In addition, many studies have established a relation between soil moisture and NO emissions (Carden et al., 1993; Zheng et al., 2000; Schindlbacher et al., 2004; Huber et al., 2020). The potential contribution of soil NO_x emissions, inferred from CHASER simulations, is discussed in section 3.3.2.

https://doi.org/10.5194/acp-2022-25
Preprint. Discussion started: 17 March 2022
© Author(s) 2022. CC BY 4.0 License.

Atmospheric Chemistry and Physics Discussions

375 **Table 4:** The number of fire events occurring during the dry season (January to April) in Phimai from
376 2015 to 2018. The selection criteria of the data are – (1) situated within 100 km of the site, (2) confidence
377 level > 70%, and (c) daytime measurements.

Dry season years	Number of fire events
2015	84
2016	98
2017	62
2018	77

378
379
380

381 **3.1.3.1 The HCHO to NO_2 ratio (R_{FN}):**

382 The HCHO to NO_2 (R_{FN}) ratio is considered as an indicator of high ozone O_3 sensitivity (Martin et al.,
383 2004; Duncan et al., 2010). The O_3 production regime is characterized as VOC-limited for $R_{FN} < 1$ and
384 NO_x- limited when $R_{FN} > 2$, and the values in the range 1-2 are said to be in the transition/ambiguous
385 region (Duncan et al., 2010; Ryan et al., 2020). After Tonnesen and Dennis (2000), several studies
386 utilized R_{FN} estimated from satellite and ground-based observations to infer O_3 sensitivity to NO_x and
387 VOCs (Irie et al.,2021; Jin and Holloway et al.,2015; Mahajan et al., 2015; Duncan et al., 2010; Martian
388 et al., 2004; etc.). However, the effectiveness of R_{FN} is still under discussion primarily based on two-
389 points- (1) the range of the transition region to categorize the VOC and NO_x -limited region, and (2) the
390 altitude dependence of R_{FN} (i.e., Jin et al. 2017). Most of the studies mentioned above used the transition
391 range ($1 < R_{FN} < 2$) proposed by Duncan et al. (2010). Schroeder et al. (2017) reported that a common
392 transition (i.e., $1 < R_{FN} < 2$) range might not be valid globally and should be calculated based on region.
393 At first, the results based on the standard transition range are discussed here, and then its applicability in
394 the study regions is inferred.
395 Figure 5 shows scatter plots of daily mean NO_2 and HCHO concentrations in the 0-2 km layer at the three
396 sites, color-coded with the respective O_3 concentrations (0-2 km). Retrieval of the JM2 O_3 product is
397 explained in Irie et al. (2011). The O_3 concentrations for SZA < 50° are used to minimize stratospheric

https://doi.org/10.5194/acp-2022-25
Preprint. Discussion started: 17 March 2022
© Author(s) 2022. CC BY 4.0 License.

Atmospheric Chemistry and Physics Discussions

effects. The JM2 O_3 product showed good agreement with ozonesonde measurements (Irie et al., 2021). The R_{FN} values for HCHO concentrations < 10 ppbv are shown, because the transition range $1 < R_{FN} < 2$ is valid for HCHO concentrations < 10 ppbv (Souri et al., 2020). Most of the high O_3 occurrences fall in the $R_{FN} > 2$ region at Phimai and Pantnagar and in $R_{FN} < 1$ at Chiba. The common transition range classifies the O_3 production regime as NO_x-limited in Phimai and Pantnagar and VOC-limited in Chiba. The change of the upper limit of the HCHO concentrations does not significantly affect the results (Fig. S1 in the supplementary information). At all sites, the R_{FN} values tend to be biased to a particular regime (i.e., NO_X - or VOC-limited), with only 4 and 2% of the ratios in the range 0-2, in Phimai and Pantnagar, respectively. This suggests that the transition occurs at higher or lower ratios than the common definition. The recent work of Souri et al. (2020) found that the NO_2-HCHO relationship plays an important role in determining the transition region and derived a formulation from accounting for the NO_2-HCHO chemical feedback in the ratios as follows:

$$HCHO = m * (NO_2 - b) \quad (6)$$

where m and b are the slope and intercept. Equation (6) is based on observations, which means the regionally adjusted fitting coefficients will reflect the local NO_2 - HCHO relationship. Solving equation (6), the transition line estimated from the observations in the 0-2 km layer, is shown in Fig 6. Rather than a range, the method calculates a single transition line, which corresponds to the NO_2-HCHO feedback. The regions above and below the transition line are characterized as VOC- and NO_x -limited or other, respectively.

https://doi.org/10.5194/acp-2022-25
Preprint. Discussion started: 17 March 2022
© Author(s) 2022. CC BY 4.0 License.

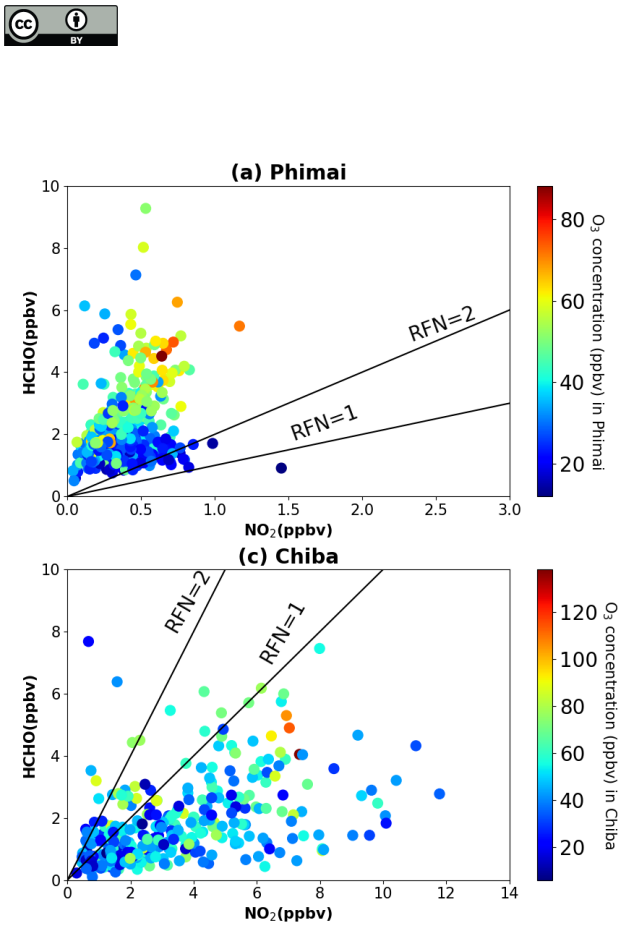

Figure 5. The scatter plot of HCHO and NO_2 concentrations in the 0-2 km layer at (a) Phimai, (b) Pantnagar, and (c) Chiba, colored with the O_3 concentrations in the 0-2 km layer at the respective sites. The solid lines indicate R_{FN} = 2 and R_{FN} =1 benchmark.

https://doi.org/10.5194/acp-2022-25
Preprint. Discussion started: 17 March 2022
© Author(s) 2022. CC BY 4.0 License.

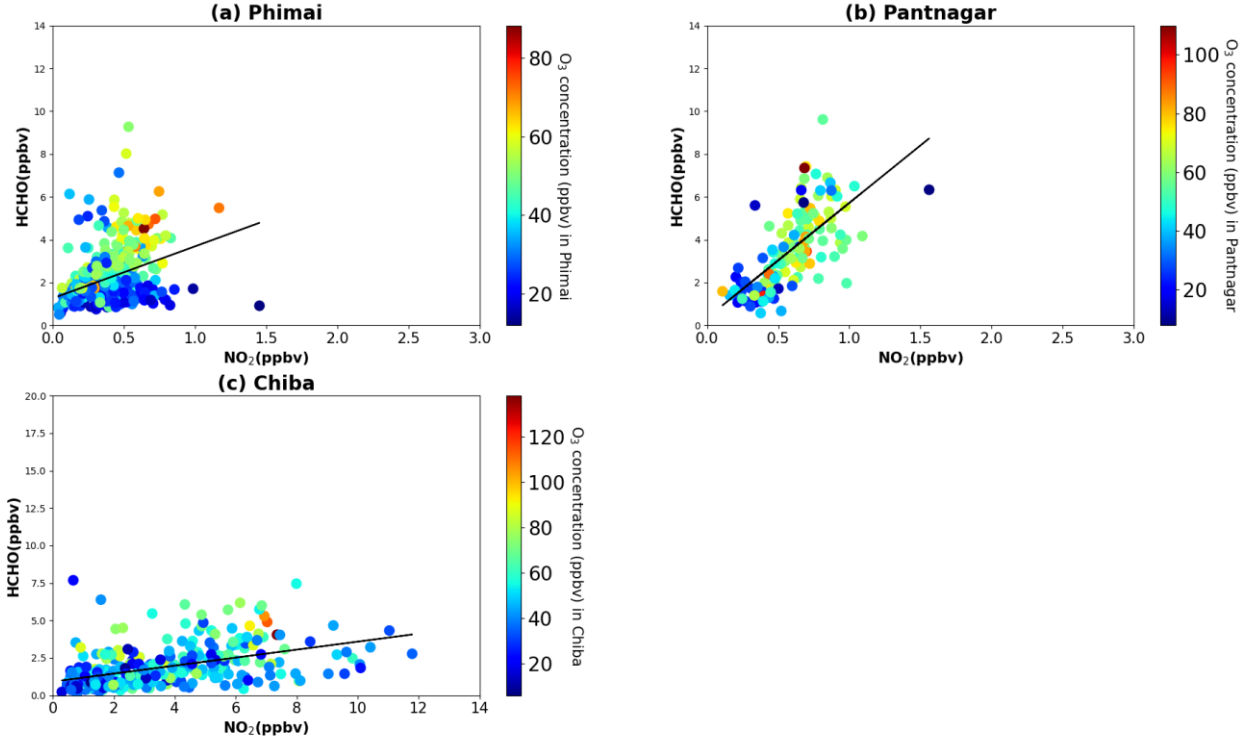

Figure 6. The scatter plot of HCHO and NO_2 concentrations in the 0-2 km layer at (a) Phimai, (b) Pantnagar, and (c) Chiba, colored with the O_3 concentrations in the 0-2 km layer at the respective sites. The solid lines indicate the transition lines calculated adopting the method of Souri et al. (2020).

The revised transition line in Phimai and Pantnagar seems to be more reasonable than Fig. 5. In Phimai, the transition line almost clearly distinguishes between the high and low O_3 occurrences. It is perceptible that when the HCHO concentrations are higher than NO_2, the transition of the regimes is likely to occur at higher R_{FN} values. The minimum and mean R_{FN} value along the transition line is 3.62 and 6.78, respectively. Because Phimai is a VOC-rich environment, the regime transition occurs at higher R_{FN} values than the conventional definition. This echoes the results of Schroder et al. (2017) on a regionally variable transition region. The definition of R_{FN} <1 as a VOC -limited regime might not be valid in this case. Considering the mean R_{FN} ratio along the transition line (i.e., 6.78), the VOC- and NO_x -limited (and other) regimes are defined as R_{FN} <6.78 and R_{FN} >6.78, respectively. Based on this definition, around 34% (65%) of the ratios are higher (lower) than 6.78, classifying Phimai as a dominant VOC-limited region,

https://doi.org/10.5194/acp-2022-25
Preprint. Discussion started: 17 March 2022
© Author(s) 2022. CC BY 4.0 License.

Atmospheric Chemistry and Physics Discussions

436 which contradicts earlier results (Fig. 5). Biomass burning affects Phimai from January to April and is a
437 significant emission source besides biogenic emission. Thus, high O_3 occurrences likely occur only 30%
438 of the time in a year, and such events are mostly lying above the transition line.
439 In Pantnagar, high O_3 occurrences lie below (42%) and above (57%) the transition line, indicating that O_3
440 production is sensitive to both HCHO and NO_2 , which contradicts Biswas et al. (2019). Pantnagar is a
441 sub-urban site situated beside a busy road. Therefore, the effect of the anthropogenic emissions is
442 expected year-round and the pyrogenic emissions during the spring and post-monsoon period. The O_3
443 sensitivity to both NO_x and VOCs in the northwest IGP region has also been reported in Kumar and Sinha
444 (2021). The mean and minimum R_{FN} value along the transition line is 5.59 and 6.09. The minimum value
445 (i.e., 5.59) is higher than Phimai (3.26), suggesting higher VOC levels in Pantnagar, consistent with the
446 observations.
447 In Chiba, 60% of the R_{FN} values lie below the transition line, suggesting a dominant VOC-limited
448 region, consistent with the results of Irie et al. (2021). The minimum and the mean R_{FN} along the transition
449 line are 0.33 and 0.72, respectively. The transition occurs at a low R_{FN} value due to higher NO_2 levels.
450 Around 40% of the R_{FN} values above the transition region suggest a moderate impact of HCHO on the
451 ozone sensitivity in Chiba.
452 Although the new classification results seem to be reasonable, they should be interpreted with care.
453 Our current understanding of R_{FN} contradicts the classification of rural sites as VOC-limited. Despite the
454 theoretical and observational evidence (i.e., Souri et al.,2020), the classification of regimes based on a
455 single transition line is not yet well-established. Schroder et al. (2017) used regionally varying transition
456 ranges. Moreover, (a) the number of observations and (b) the systematic and retrieval errors can impact
457 the estimations and classifications. These findings are expected to contribute to the ongoing discussion
458 on the effectiveness of R_{FN}. However, the results clarify the idea of a regionally varying transition range.
459
460
461
462 **3.1.3.2 R_{FN} profiles**

https://doi.org/10.5194/acp-2022-25
Preprint. Discussion started: 17 March 2022
© Author(s) 2022. CC BY 4.0 License.

Atmospheric Chemistry and Physics Discussions

Figure 7 shows the seasonal mean R_{FN} profiles at the three sites. The profiles during the high O_3 concentrations at the sites (i.e., March in Phimai, May in Pantnagar, and February in Chiba) are only shown. The R_{FN} values will likely increase with height, because of the lower vertical gradient of NO_2, compared to HCHO (Fig. 4). Interestingly, the R_{FN} values are almost similar in the 1-2 km height under biomass burning conditions, suggesting a small variability in the HCHO loss rate in the particular layer. At both sites, the HCHO concentration at 1.5 km is about 3 ppbv. In Chiba, a significant amount of NO_2 in the higher layers increases the ratio up to 2 km. Above 2 km, the ratio variability at all sites is opposite the surface. The gradient issue of R_{FN} has been discussed explicitly by Jin et al. (2017). They proposed a conversion factor to account for gradient differences in the surface and column-derived R_{FN} values, estimating the conversion factor from the model simulated surface and column abundances of NO_2 and HCHO. We adopt the method reported by Jin et al. (2017) for this study using the CHASER simulated NO_2 and HCHO concentrations and vertical columns.

First, the CHASER simulated near-surface NO_2 and HCHO concentrations were converted to number density, and the effective boundary layer height (E) (Halla et al., 2011; Jin et al., 2017) was estimated.

$$E_{NO_2} = \frac{NO_2\ total\ column}{NO_2\ near-surface\ number\ density} \quad (7)$$

$$E_{HCHO} = \frac{HCHO\ total\ column}{HCHO\ near-surface\ number\ density} \quad (8)$$

Therein, E_{NO_2} and E_{HCHO} respectively denote the effective boundary layer heights of NO_2 and HCHO. In the second step, the column to surface conversion factor (F) was calculated according to the following equation:

$$F = \frac{E_{HCHO}}{E_{NO_2}} \quad (9)$$

The seasonal variation of F for the three A-SKY sites and the associated 1σ standard deviation of the mean values are depicted in Fig. 7(c). The F values over East Asia reported by Jin et al. (2017) were ~2, with no marked seasonal variation. Compared to values reported in the literature, the CHASER estimated

https://doi.org/10.5194/acp-2022-25
Preprint. Discussion started: 17 March 2022
© Author(s) 2022. CC BY 4.0 License.

Atmospheric Chemistry and Physics Discussions

F values over Chiba range between 1–2.5, which seems reasonable despite the coarse resolution of CHASER. The literature values are reported for polluted regions (NO_2 > 2.5 molecules cm^{-2}) and considered the simulation data for 1–2 PM, whereas the estimates of this study used daytime (07:00 – 18:00) simulation.

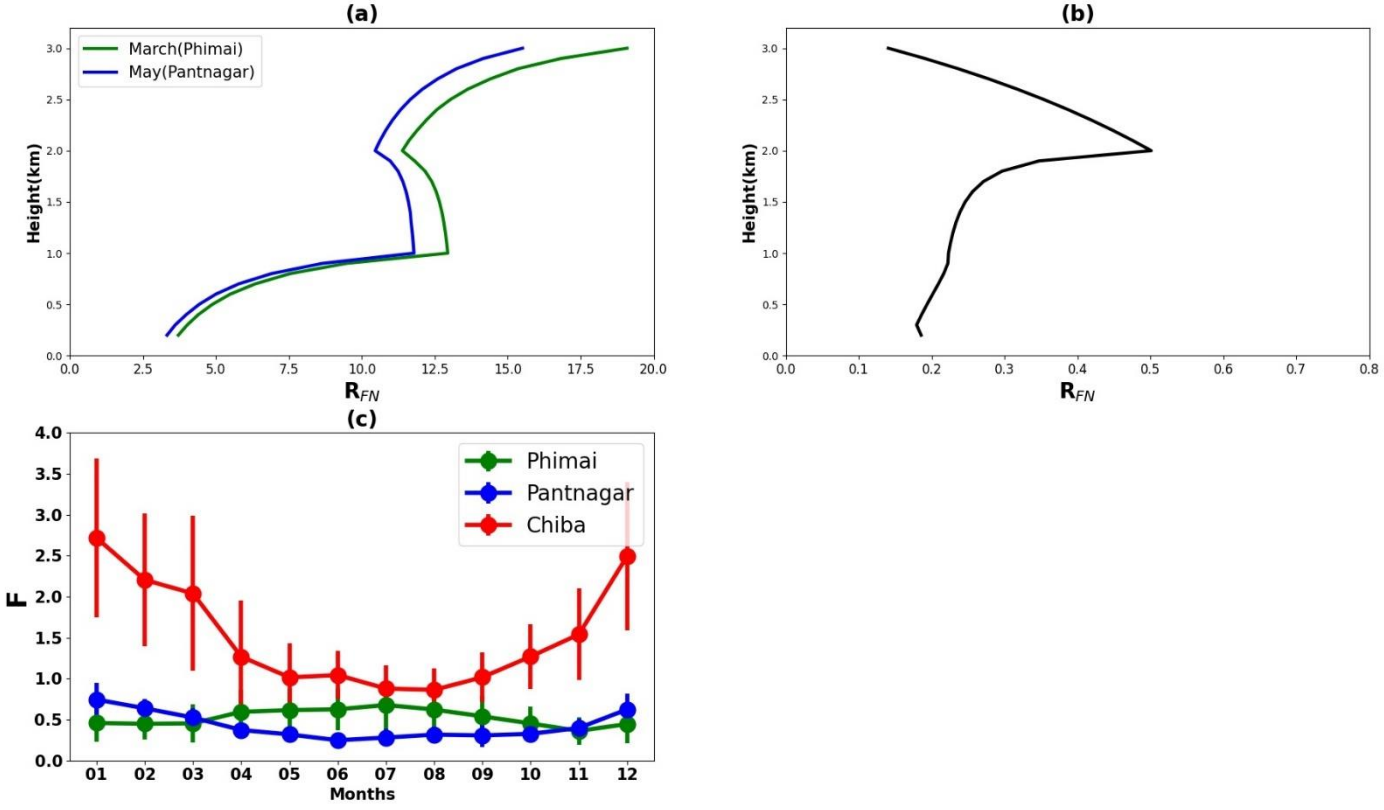

Figure 7: The seasonal mean R_{FN} profiles during (a) March and May in Phimai and Pantnagar, respectively, and (b) February in Chiba. The months corresponding to the high O_3 concentrations at the respective sites. (c) The seasonal variations in the column to surface conversion factor (F) for the Phimai, Pantnagar, and Chiba sites, estimated from the CHASER simulated HCHO and NO_2 surface concentrations and VCD. The simulated data from 07:00 – 18:00 in 2017 were used to estimate the F values. The error bars indicate the one sigma standard deviation of the mean values.

https://doi.org/10.5194/acp-2022-25
Preprint. Discussion started: 17 March 2022
© Author(s) 2022. CC BY 4.0 License.

Atmospheric Chemistry and Physics Discussions

The F values in Pantnagar are mostly < 1, with no distinctive seasonal variation. Mahajan et al. (2015) reported OMI-derived R_{FN} values < 1 over the IGP region. When this estimated conversion factor is used with the values of Mahajan et al. (2015), the discrepancy in the satellite and ground-based observation derived R_{FN} values in the IGP region are reduced, indicating that the estimated F values for the Pantnagar site can be representative for the IGP region. The F values at the Phimai site range were 0.5–1. No report of the relevant literature presents F values for the southern and southeastern Asian regions. Consequently, our estimated F values for the Phimai and Pantnagar sites are useful as representative values for these respective regions, which can be improved further based on the results.

3.2 Evaluation of CHASER simulations at the three sites

3.2.1 Evaluation of CHASER HCHO in Phimai and Chiba

The seasonally averaged observed and modeled HCHO profiles and partial columns in the 0-4 km altitude range in Phimai and Chiba are shown in Fig. 8. The CHASER outputs smoothed with MAX-DOAS averaging kernels (AK) are also depicted. The AK is applied following Franco et al. (2015). First, the CHASER HCHO profiles are interpolated to the MAX-DOAS vertical grids. Next, the MAX-DOAS AK information from individual retrieved profiles is seasonally averaged according to the climate classifications of each site. Finally, the CHASER outputs on the coincident days is selected, and the AK is applied to the daily mean interpolated profile. The coincident days at Phimai and Chiba were 690 and 668, respectively. The comparisons at the Pantnagar site are discussed separately.

At the Phimai, CHASER predicted the increase in the HCHO partial columns during the dry season and well-reproduced the HCHO seasonality, with an *R*-value of 0.96. The modeled monthly mean values during the dry season are within the 1σ standard deviation of the observed values, indicating the pyrogenic emissions estimates used for the simulations are reasonable. CHASER predicted a 41% increase in the HCHO column from January to March, consistent with the observations (41%). CHASER overestimates the HCHO columns in both seasons, and the mean bias error (MBE) (CHASER – MAX-DOAS) is lower (3.7×10^{15} molecules cm^{-2}) (Table 5) in the wet season. Although underestimated, the dry season smoothed column values are within the 1σ range.

https://doi.org/10.5194/acp-2022-25
Preprint. Discussion started: 17 March 2022
© Author(s) 2022. CC BY 4.0 License.

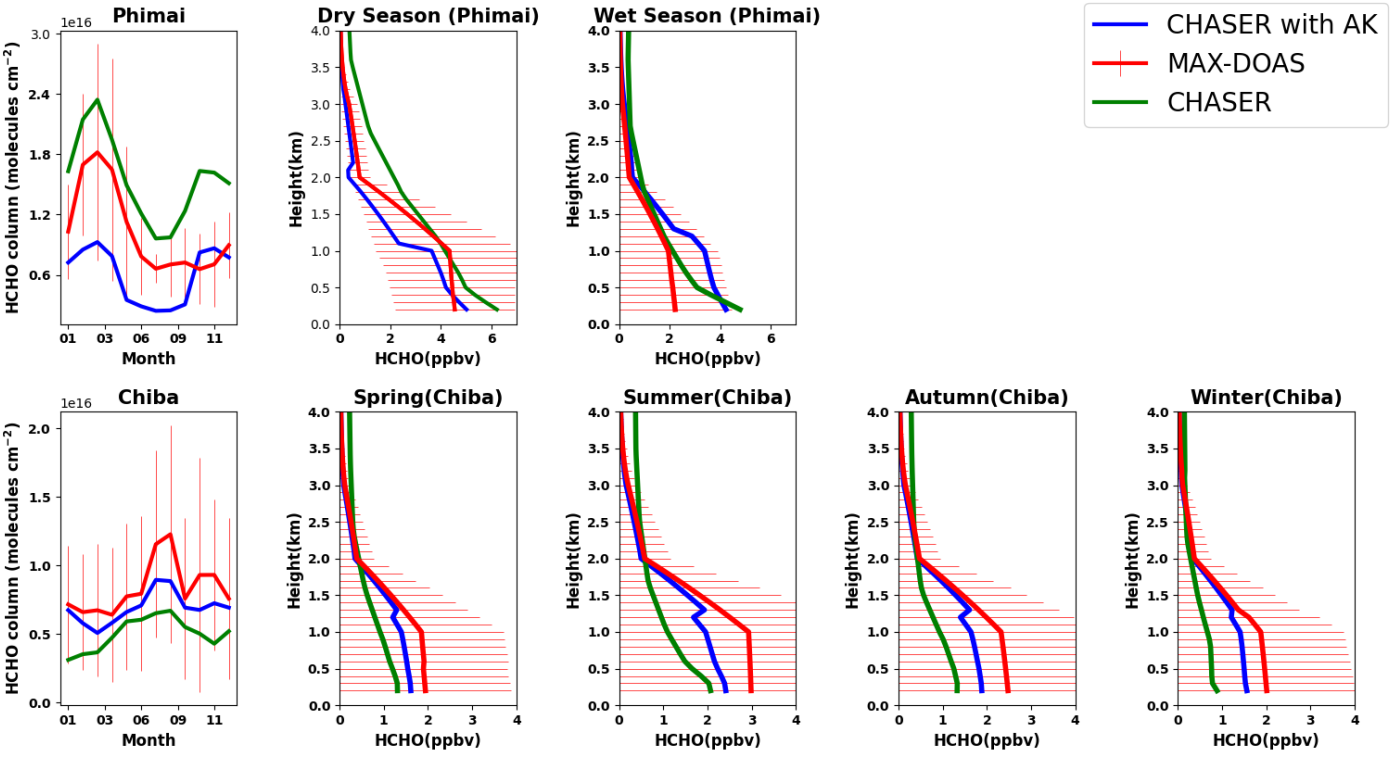

527 **Figure 8.** The seasonal variations in the HCHO partial columns from 0 to 4 km and vertical profiles during all
528 seasons at Phimai and Chiba, inferred from the MAX-DOAS observations (red) and CHASER simulation(green).
529 The CHASER HCHO partial column and vertical profile smoothed with the MAX-DOAS AK are colored in blue.
530 The AK information of all the screened (as explained in section 2.2) retrievals were averaged based on the seasonal
531 classification of the respective sites. The coincident time and date between the model and observations are selected
532 only. The error bars indicate the one sigma standard deviation of mean values of the MAX-DOAS observations.
533

534 The modeled and observed HCHO concentrations in the 1- 2km layers during the wet season are almost
535 identical, whereas concentrations near the surface (i.e., 0-1 km) differ by 30%. The absolute mean
536 difference in the 0-4 km layer is ~0.45ppbv, with the maximum difference of 2.58 ppbv below 200 m.
537 CHASER has demonstrated good skills in reproducing the HCHO profile in the 0.5 – 4 km layer during
538 the wet season. The significance of AK information is low for the wet season; however, smoothing the
539 model profiles reduces the overall MBE by 43%.
540

https://doi.org/10.5194/acp-2022-25
Preprint. Discussion started: 17 March 2022
© Author(s) 2022. CC BY 4.0 License.

Atmospheric Chemistry and Physics Discussions

Table 5: Comparison of the seasonal mean HCHO partial columns and profiles (0-4 km) between MAX-DOAS and CHASER at Phimai and Chiba. MBE (CHASER – MAX-DOAS) is the mean bias error. The partial column and profile MBE units are $\times 10^{16}$ molecules cm^{-2} and ppbv, respectively.

Site	Season	Partial column MBE	Smoothed Partial column MBE	Profile MBE	Smoothed Profile MBE
Phimai	Overall	0.28	-0.07	0.35	0.01
Phimai	Dry	0.37	-0.28	0.58	-0.38
Phimai	Wet	0.21	0.07	0.45	0.33
Chiba	Overall	-0.12	-0.05	-0.37	-0.11
Chiba	Spring	-0.07	-0.04	-0.22	-0.12
Chiba	Summer	-0.16	-0.08	-0.45	-0.26
Chiba	Autumn	-0.10	-0.04	-0.40	-0.19
Chiba	Winter	-0.09	-0.01	-0.42	0.11

During the dry season, the absolute mean and maximum difference in the datasets in the 0-1 km layers is ~1ppbv and ~2ppbv, respectively. The observed and simulated seasonal differences in the 0-1 km are 50 and 34%, respectively. Simulated dry season profile values above ~2 km is out of the 1σ variability range. The two-potential reasons for such differences are lower measurement sensitivity in the free troposphere and overestimated biogenic emissions in the model. Despite the measurement limitations, CHASER and MAX-DOAS wet season profiles up to 3km are consistent. Thus, it is likely that the biogenic emissions in the model are overestimated. However, the dry season HCHO profiles in 0-2 km are well simulated. The smoothing underestimates the dry season profile within the 1σ variability range but improved simulations below 200 m. Above 3 km, the smoothed values mostly imitate the apriori due to reduced measurement sensitivity (i.e., low AK value, indicating limited information could be retrieved).

A moderate correlation (R=0.58) is observed between the modeled and observed HCHO partial columns at Chiba. CHASER could reproduce the peak in the partial columns in August. The model

https://doi.org/10.5194/acp-2022-25
Preprint. Discussion started: 17 March 2022
© Author(s) 2022. CC BY 4.0 License.

Atmospheric Chemistry and Physics Discussions

predicts a 41% increase in the HCHO columns from January to August, whereas the observed increase is 54%. Although Chiba is an urban site, the HCHO and temperature seasonal variations show a tight correlation (R~ 0.70) (Fig S2), suggesting changes in biogenic emissions modulates HCHO seasonality. Similarly, the modeled seasonality is consistent with temperature variability (Fig. S2). Thus, the simulated HCHO seasonality in Chiba is reasonable, despite underestimated absolute values. Smoothing the simulations improves the correlation, and the MBE is reduced by 54% (Table 4).

The CHASER HCHO profiles in the 0- 4 km layers are lower than the observations, with an MBE of 0.39 ppbv. The absolute differences in the modeled and retrieved HCHO profiles in the 0-2 km layer during all seasons are higher than in Phimai. Absolute mean differences ~ 1pbbv and higher mainly are observed from 0 to 2 km. In addition, the vertical gradients of the simulated profiles are low compared to Phimai. The modeled profiles in Chiba resemble the HCHO profiles measured over the ocean during the INTEX-B (Intercontinental Chemical Transport Experiment: Phase B) (Boeke et al., 2011). The Chiba site is near the sea, and coarse CHASER resolution includes the ocean pixels. Moreover, urban surfaces are not homogeneous. Thus, a significant part of the profile discrepancies is likely related to the systematic differences, in addition to emission estimates. However, the model estimates lie within the standard deviation range of the measurements. Due to the low gradients in the simulated profiles, the smoothed profiles mostly imitated the a priori values even below 2 km. The impact of the horizontal resolution on the simulated HCHO levels is discussed in section 3.2.4.

3.2.2 Evaluation of CHASER NO_2 in Phimai and Chiba

Figure 9 presents the seasonal averages of the MAX-DOAS and CHASER NO_2 profiles and partial columns (0-4 km) in Phimai and Chiba. The AK is applied to the modeled outputs for the Chiba site only.

https://doi.org/10.5194/acp-2022-25
Preprint. Discussion started: 17 March 2022
© Author(s) 2022. CC BY 4.0 License.

Atmospheric Chemistry and Physics Discussions

Figure S3 in the supplementary information compares the observations, model, and smoothed model profiles averaged within the 0-2 km layer in Phimai. The smoothing with different apriori values is depicted to demonstrate the impact of the apriori values. The smoothed NO_2 concentrations, calculated using the original a priori values, show a seasonal variation shift. The mean smoothed profile resembles the observations when apriori values are reduced by 50%; however, the dry season values are similar in both cases. The apriori values are sensitive to the surface because a priori data are taken from the retrieved VCD and SCD values. Two test cases of smoothing profiles utilizing apriori values above 500 and 800 m shows good agreement with the observations; however, the results are sensitive to the apriori values. Because smoothed profiles are strongly biased to the apriori choice, the smoothing results for the Phimai site are discarded.

The modeled NO_2 partial column in Phimai shows good agreement with the observations during the dry season. CHASER well reproduces the enhanced NO_2 columns due to biomass burning within the standard deviation of the observations. The peak in the NO_2 levels during March is consistent in both datasets. Although the seasonality does not agree in other months, the overall MBE is 8×10^{13} molecule cm^{-2} (Table 6). Above 500 m, the datasets shows excellent agreement. The absolute mean differences in the 0-1km layer are 0.22 ppbv, and the maximum difference of ~1.9 ppbv is observed near the surface. Amidst the biomass burning influence, the NO_2 concentrations in Phimai are mostly < 1 ppbv. Thus, the comparison results demonstrate CHASER's good skills in a region characterized by low NO_2 concentrations. Moreover, when NO_2 concentrations are less than < 1 ppbv, the AK information seems less significant if the model can capture low concentration scenarios.

https://doi.org/10.5194/acp-2022-25
Preprint. Discussion started: 17 March 2022
© Author(s) 2022. CC BY 4.0 License.

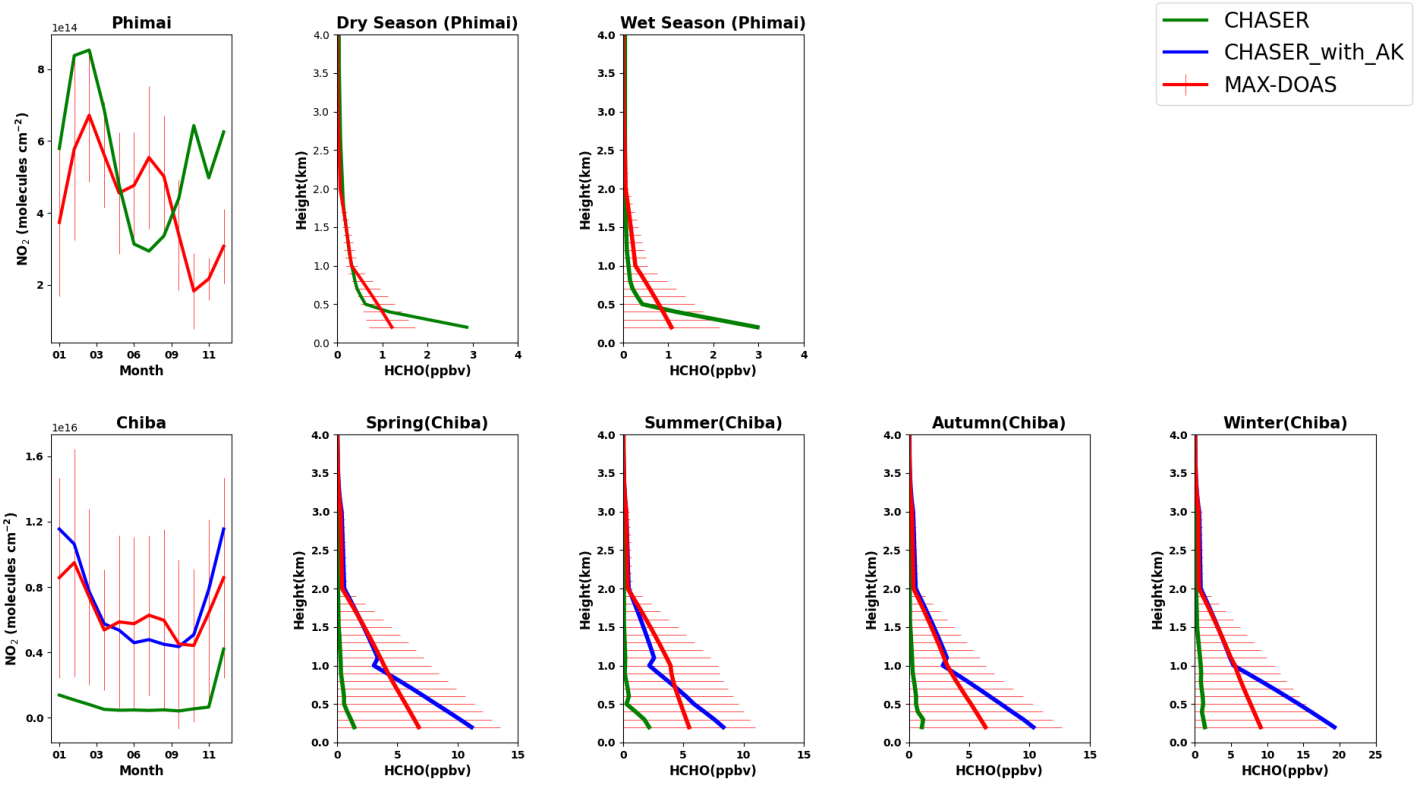

Figure 9. The seasonal variations in the NO_2 partial columns from 0 to 4 km and vertical profiles during all seasons at Phimai and Chiba, inferred from the MAX-DOAS observations (red) and CHASER simulation(green). The CHASER NO_2 partial column and vertical profile smoothed with the MAX-DOAS AK are colored in blue. The coincident time and date between the model and observations are selected only. The error bars indicate the one sigma standard deviation of mean values of the MAX-DOAS observations.

https://doi.org/10.5194/acp-2022-25
Preprint. Discussion started: 17 March 2022
© Author(s) 2022. CC BY 4.0 License.

Atmospheric Chemistry and Physics Discussions

621 **Table 6:** Comparison of the seasonal mean NO_2 partial columns and profiles (0-4 km) between MAX-DOAS and
622 CHASER at Phimai and Chiba. MBE (CHASER – MAX-DOAS) is the mean bias error. The partial column and
623 profile MBE units are $\times 10^{15}$ molecules cm^{-2} and ppbv, respectively.

Site	Season	Partial column MBE	Smoothed Partial column MBE	Profile MBE	Smoothed Profile MBE
Phimai	Overall	0.08		0.11	
Phimai	Dry	0.18		0.09	
Phimai	Wet	-0.14		0.02	
Chiba	Overall	-5.58	-1.90	-3.27	-1.66
Chiba	Spring	-5.56	-2.00	-3.19	-1.74
Chiba	Summer	-5.52	-2.87	-2.85	-1.86
Chiba	Autumn	-4.57	-1.24	-2.74	-1.40
Chiba	Winter	-6.64	-1.50	-4.30	-1.63

624

625 Although the datasets are moderately correlated (R=0.59) in Chiba, the model largely underestimates the
626 NO_2 partial column with MBE of ~5×10^{15} molecules cm^{-2}. The model predicts almost constant NO_2
627 profiles and columns throughout the year, and thus the respective seasonal biases are almost similar. The
628 vertical gradient of the modeled NO_2 profiles is low, too, similar to the HCHO profiles. The model
629 resolution could be a potential case of such significant underestimation. The AKs significantly improved
630 the partial column and profiles, reducing the MBE by more than 50%; however, the apriori values strongly
631 affect the smoothed profiles.

632

633 The mean NO_2 concentrations in the 0-2 km layer in 2018, simulated at the spatial resolution of 2.8˚ ×
634 2.8˚ (standard) and 1.4˚ × 1.4˚ are compared with observations in Chiba, depicted in Fig.10(a). The error
635 bars are the 1σ standard deviation of the observations. Higher resolution simulations reduced the overall
636 MBE by 35% (Table 7). NO_2 concentrations at 1.4˚ are now within the variability of the observations.
637 The 1.4˚ simulation captured the NO_2 seasonal variability better than at 2.8˚. Despite an improved
638 resolution, the model values are underestimated, with the highest MBE during the winter. According to
639 Miyazaki et al. (2020), the seasonality in the anthropogenic emissions, primarily wintertime heating, is

https://doi.org/10.5194/acp-2022-25
Preprint. Discussion started: 17 March 2022
© Author(s) 2022. CC BY 4.0 License.

Atmospheric Chemistry and Physics Discussions

not included in the emission inventories, which could likely underestimate the wintertime NO_2 levels. The best agreement between the datasets is observed during summer and spring, with an MBE of ~1 ppbv on a seasonal scale.

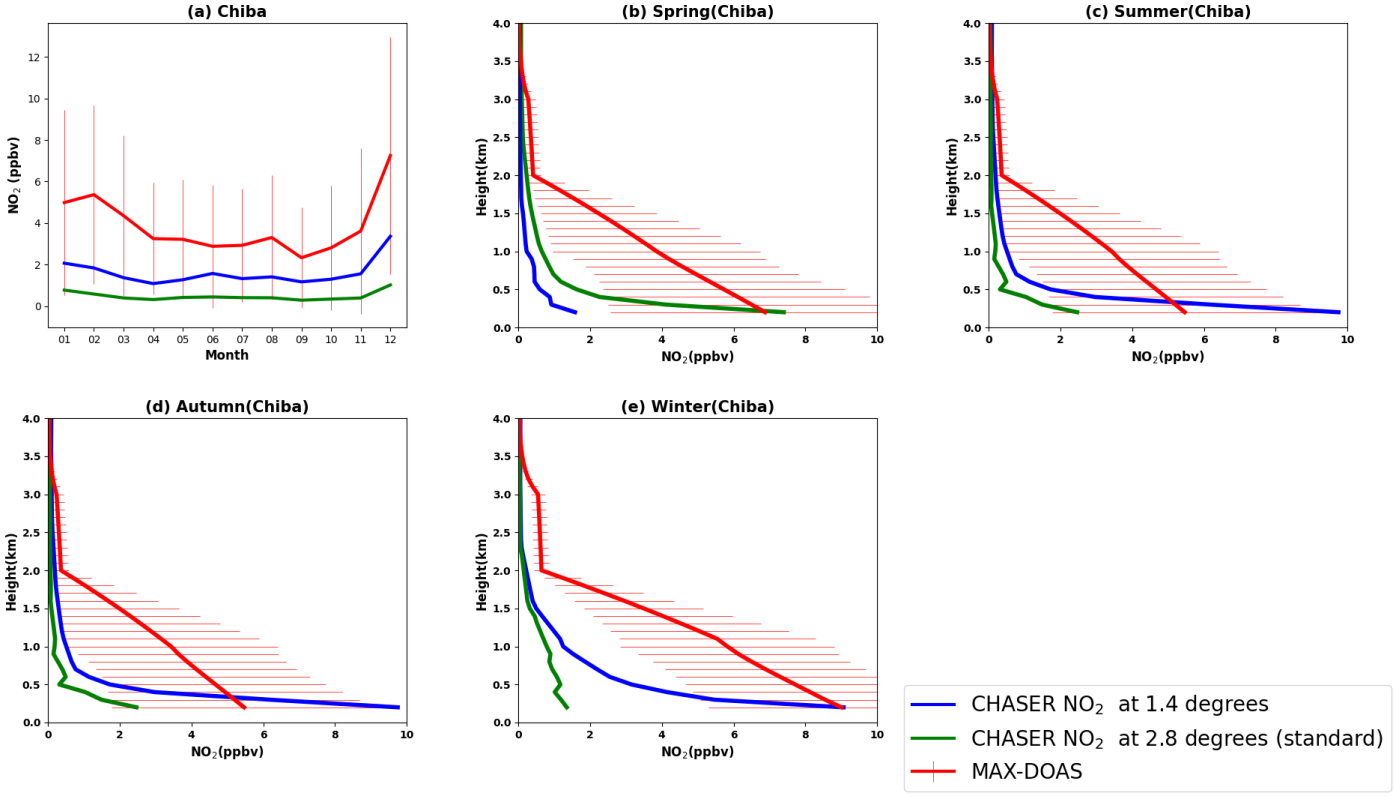

Figure 10: (a) The seasonal variations in the NO_2 concentrations in the 0-2 km layer in Chiba, inferred from the MAX-DOAS observations (red) and two CHASER simulations at 2.8˚(green) and 1.4˚(blue) resolutions. The simulated NO_2 profiles at 2.8˚(green) and 1.4˚(blue) resolutions during (b) spring, (c) summer, (d) autumn, and (e) winter are plotted with the observed seasonal profiles in Chiba. Only the data (both observed and simulated) for 2018 are plotted. The coincident time and date between the model and observations are selected only. The error bars in (a), (b), (c), and (d) indicate the one sigma standard deviation of mean values of the MAX-DOAS observations.

https://doi.org/10.5194/acp-2022-25
Preprint. Discussion started: 17 March 2022
© Author(s) 2022. CC BY 4.0 License.

Atmospheric Chemistry and Physics Discussions

653

654 NO_2 profiles at 2.8˚ and 1.4˚ resolution are evaluated in Fig. 10(b-e). The significant impact of the
655 increased resolution is observed below 500 m, reducing the negative bias by 70% near the surface. Above
656 500 m, the effect of the higher resolution is limited, with an MBE reduction of 12% in the 0.6 – 2 km.
657 Although the near-surface NO_2 concentrations at 1.4˚ resolution are overestimated, the values are within
658 the standard deviation of the observations. Around 200m, the wintertime mean NO_2 concentrations at 1.4˚
659 resolution are identical to the observations (~9 ppbv), and the summertime mean is overestimated.
660 Moreover, the NO_2 levels above 2km are similar at both resolutions. The resolution effect on NO_2 profiles
661 varies with location and season (Williams et al., 2017). For example, CHASER NO_2 at 1.1˚ resolution
662 significantly improved the agreement with aircraft observations below 650 hPa over Denver metropolitan
663 area (Sekiya et al. 2018), whereas, in Chiba, the 1.4˚ resolution improved the surface estimates. Thus, the
664 horizontal resolution is not the only reason for the model underestimation. Other factors such as the
665 vertical resolution, uncertainties in emission inventories, chemical kinetics, etc., can also affect the
666 simulated NO_2 estimates. The impact of the emission inventory is discussed in section 3.2.4.

667

668 **Table 7:** Comparison of the seasonal mean NO_2profiles (0-2 km) among MAX-DOAS and CHASER simulations
669 at 2.8˚ and 1.4˚ resolutions at Chiba. MBE at (CHASER – MAX-DOAS) 1.4˚ and 2.8˚ are the mean bias error at
670 the respective resolutions. The MBE unit is ppbv.

Season	**MBE at 1.4˚**	**MBE at 2.8˚**
Overall	-2.24	-3.37
Spring	-2.26	-3.23
Summer	-1.50	-2.47
Autumn	-1.57	-2.57
Winter	-3.44	-5.07

671

672

673

https://doi.org/10.5194/acp-2022-25
Preprint. Discussion started: 17 March 2022
© Author(s) 2022. CC BY 4.0 License.

Atmospheric Chemistry and Physics Discussions

3.2.3 Evaluation of CHASER HCHO and NO_2 in Pantnagar

Mountainous terrain is located a few kilometers away from the Pantnagar site. The treatment of such complex landscapes is different in the datasets. The simulated surface height at Pantnagar is 1.7 km, whereas the radiative transfer calculations for MAX-DOAS retrievals consider a flat terrain. Such an assumption is expected to have a non-significant effect on the retrieval because the horizontal resolution of the MAX-DOAS system is ~10 km. Moreover, the MAX-DOAS HCHO products in Pantnagar showed good agreement with satellite observations (Hoque et al., 2018b). Because the MAX-DOAS observations are most sensitive between 0-2 km, the observations above 1.8 km are compared with the simulations. The observed, modeled, and smoothed mean HCHO levels in the 1.8 – 3 km layer are shown in Fig. 11 (a). The datasets differ significantly with an MBE of ~2.5ppbv, and simulated values are out of the 1σ variability range. Smoothing the model output reduced the MBE to 0.65 ppbv, which correlates well with the observation with an *R*-value of 0.66. Besides the systematic differences in the datasets, two potential factors can contribute to the significant discrepancies in the datasets- (1) similar to Phimai, the simulated HCHO levels in Pantnagar are higher than observations, indicating overestimated biogenic emissions. (2) Restricting the observation ELs to less than 10˚ reduces the sensitivity to the higher layers, affecting the concentration estimates in the upper layers.

Figure 11(b) compares the modeled HCHO simulations over the whole IGP region with the observations in Pantnagar. The observed HCHO seasonality in Pantnagar is consistent with Mahajan et al. (2015), reported for the entire IGP region. Thus, the comparison can assess the model capability in the IGP region. The comparison for 2017 is shown only because the observations were continuous and covered almost all the seasons.

https://doi.org/10.5194/acp-2022-25
Preprint. Discussion started: 17 March 2022
© Author(s) 2022. CC BY 4.0 License.

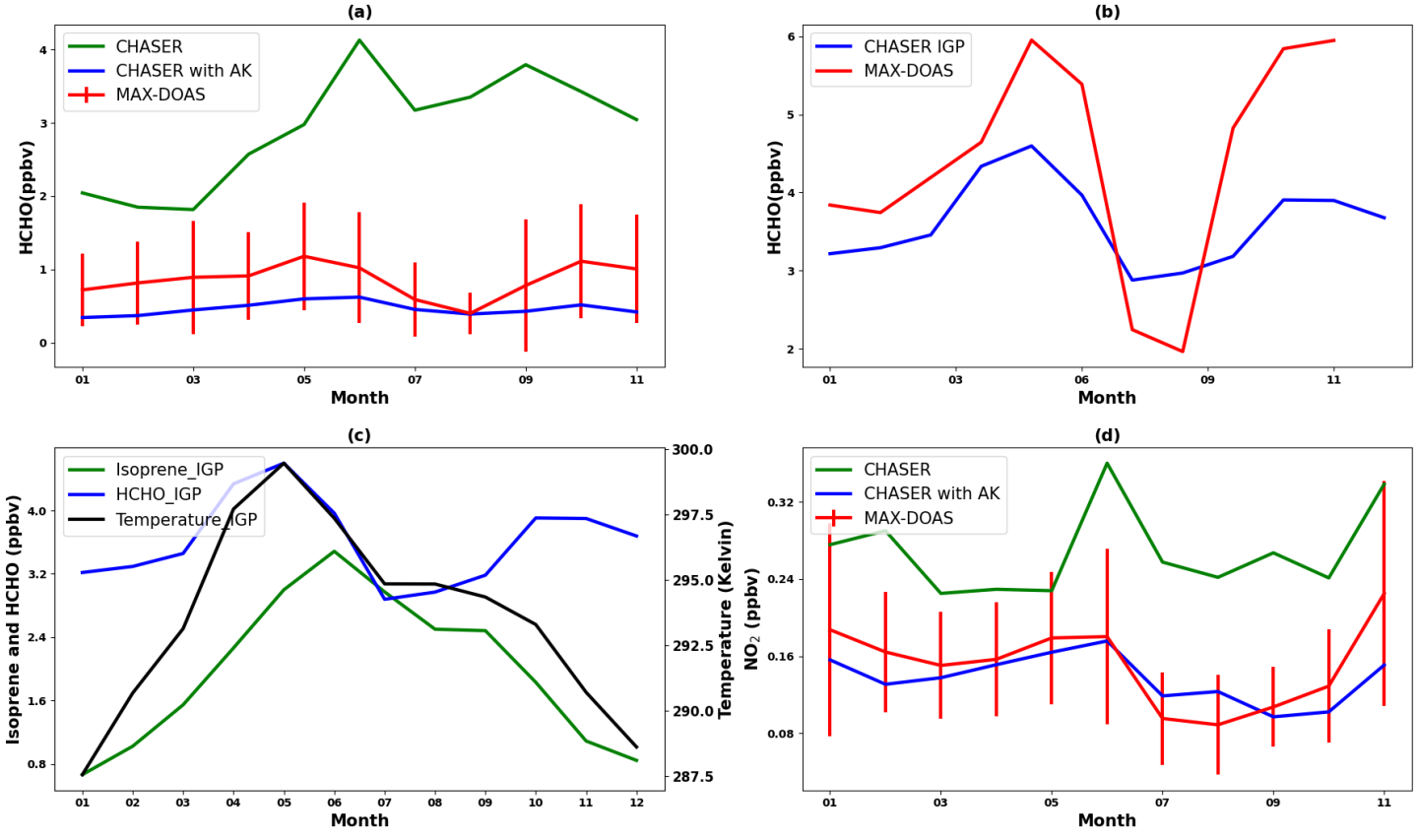

Figure 11. (top panel) (a)The seasonal variations in the HCHO concentrations in the 1.8 -3 km layer in Pantnagar, inferred from the MAX-DOAS observations (red) and CHASER simulation(green). The simulated concentrations smoothed with the MAX-DOAS AK are shown in blue. (b) The seasonal variations in the MAX-DOAS (red) and CHASER (blue) HCHO concentrations in Pantnagar and the IGP region, respectively, in 2017. The coincident dates between the observations and model are plotted only. (bottom panel) (c) The CHASER simulated seasonal variations in HCHO (blue), isoprene (green), and temperature (black) in the IGP region in 2017. Only the daytime simulated values were considered for the plot. (d) The observed (red) and modelled (green)seasonal variations in the NO_2 concentrations in the 1.8 -2 km layer in Pantnagar. The simulated concentrations smoothed with the MAX-DOAS AK are shown in blue. The error bars in (a) and (d) are the one sigma standard deviation of the observations.

https://doi.org/10.5194/acp-2022-25
Preprint. Discussion started: 17 March 2022
© Author(s) 2022. CC BY 4.0 License.

Atmospheric Chemistry and Physics Discussions

The modeled HCHO seasonal variations in the IGP region correlate well with R~ 0.80. The enhancement in the HCHO concentrations during the spring and post-monsoon season is well reproduced by CHASER. This indicates that CHASER can capture HCHO variability in complex terrains regions like IGP. Figure 11(c) depicts the isoprene concentrations and temperature in the IGP region, in addition to the HCHO concentrations. Oxidization of precursor hydrocarbon and photochemical reactions are the most dominant sources of HCHO. Isoprene is the most abundant hydrocarbon in the atmosphere. The average ambient isoprene concentrations during July, August, and September in the IGP region are 1.4±0.3 ppbv (Mishra et al., 2020). Therefore, the CHASER isoprene concentration range of 1.5–2 ppbv during the monsoon season seems reasonable. The HCHO concentrations in the IGP region reach a peak during the spring and post-monsoon seasons. A strong correlation between HCHO, isoprene, and temperature variation (R ~ 0.90) in the first half of the year indicates that the change in biogenic emissions strongly drives the HCHO seasonal modulation. The observed enhancement in the HCHO levels during spring in Pantnagar is related to biomass burning. The biomass burning events are primarily concentrated in the northwest IGP region (Kumar and Sinha, 2021), where the site is located. On a regional scale, the biomass burning impact is expected to smear. Thus, the strong effect of the biogenic emission on the regional HCHO modulation is reasonable. HCHO modulation differs from isoprene and temperature during the post-monsoon period, suggesting a more substantial role of biomass burning and anthropogenic emissions. Thus, the physical processes driving the HCHO seasonality in the IGP region are well reflected in the CHASER simulations.

The observed, modeled, and smoothed mean NO_2 levels in the 1.8 – 2 km layer are shown in Fig. 11 (d). The layers 1.8-2 km are considered instead of 1.8 – 3 km because of the lower gradient of NO_2 than HCHO (Fig. 4). Despite overestimated modeled values, the datasets are moderately correlated with R ~0.52. Smoothing the model output increases the correlation to 0.74. The model estimated seasonal modulation is 40%, whereas the observed modulation is 60%, with the maximum absolute difference of ~0.18 ppbv. CHASER could capture the NO_2 variability (<1 ppbv) in Pantnagar near the free troposphere. According to the datasets, the mean NO_2 concentrations range from 0.2 to 0.35 ppbv at 2km in Pantnagar during biomass burning events. The simulated seasonal NO_2 estimates near the free troposphere (1.8 – 2 km) are consistent with the observations at all three sites.

https://doi.org/10.5194/acp-2022-25
Preprint. Discussion started: 17 March 2022
© Author(s) 2022. CC BY 4.0 License.

Atmospheric Chemistry and Physics Discussions

735

736 **3.2.4 Impact of the model resolution and emission inventories on the results**

737 The impact of the spatial resolution on the evaluation results is assessed by comparing the CHASER
738 simulations at 2.8˚ and 1.4˚ resolutions, shown in Fig. 12. The latitude and longitude range of the averaged
739 values is 0˚-50˚ N and 60˚ – 150˚ E, respectively, covering the location of all three sites. Simulations for
740 2018 are plotted and analysed only. The two NO_2 simulations differ on average by 5%. The differences
741 in the latitude range of 28˚ – 40˚ N and 10˚ – 20˚N is around 10 and 3 %, respectively. This suggests that
742 the NO_2 comparison results in South and East Asia will improve by at least 10% at a higher resolution.
743 The discussion in section 3.2.2 showed that the resolution-based improvement in the overall profile was
744 limited and varied regionally. At a spatial resolution of 1.1˚, CHASER NO_2 columns can capture the
745 regional NO_2 climatology over polluted and biomass burning region better than at 2.8˚ (Sekiya et al.
746 2018). The biomass burning enhanced NO_2 levels were well reproduced in Phimai at 2.8˚; however, the
747 concentrations were less than 1 ppbv. NO_2 simulations at 2.8˚ were reasonable in low NO_2 regions. The
748 HCHO levels in Chiba and the rest of the region improved by around 8 and 2 %, respectively, indicating
749 low sensitivity to spatial resolution. Therefore, HCHO estimates at 1.4˚ resolution would yet be
750 underestimated in Chiba. Overall, the impact of the model resolution on the results is estimated to be
751 around 20%.

752 Although the NO_x estimates for the low NO_2 regions seem reasonable, global NO_x emissions have
753 changed since 2008(i.e., EDGAR-HTAP (2008) emissions used in this study). A recent study by Miyazaki
754 et al. (2020) reported changes in global NO_x emissions from 2005 to 2018. They found a continuous 30%
755 increase in NO_x emissions in India since 2005 and a substantial increase in Southeast and Southern Asia.
756 Thus, the current simulation settings will likely underestimate the NO_2 concentrations in these regions.
757 Figure S4 depicts the simulated and measured NO_2 concentrations in two polluted cities (Delhi and
758 Kolkata) in India. Updated NO_x estimates would yield higher NO_2 concentrations and improve the
759 comparison, yet likely to be underestimated.

https://doi.org/10.5194/acp-2022-25
Preprint. Discussion started: 17 March 2022
© Author(s) 2022. CC BY 4.0 License.

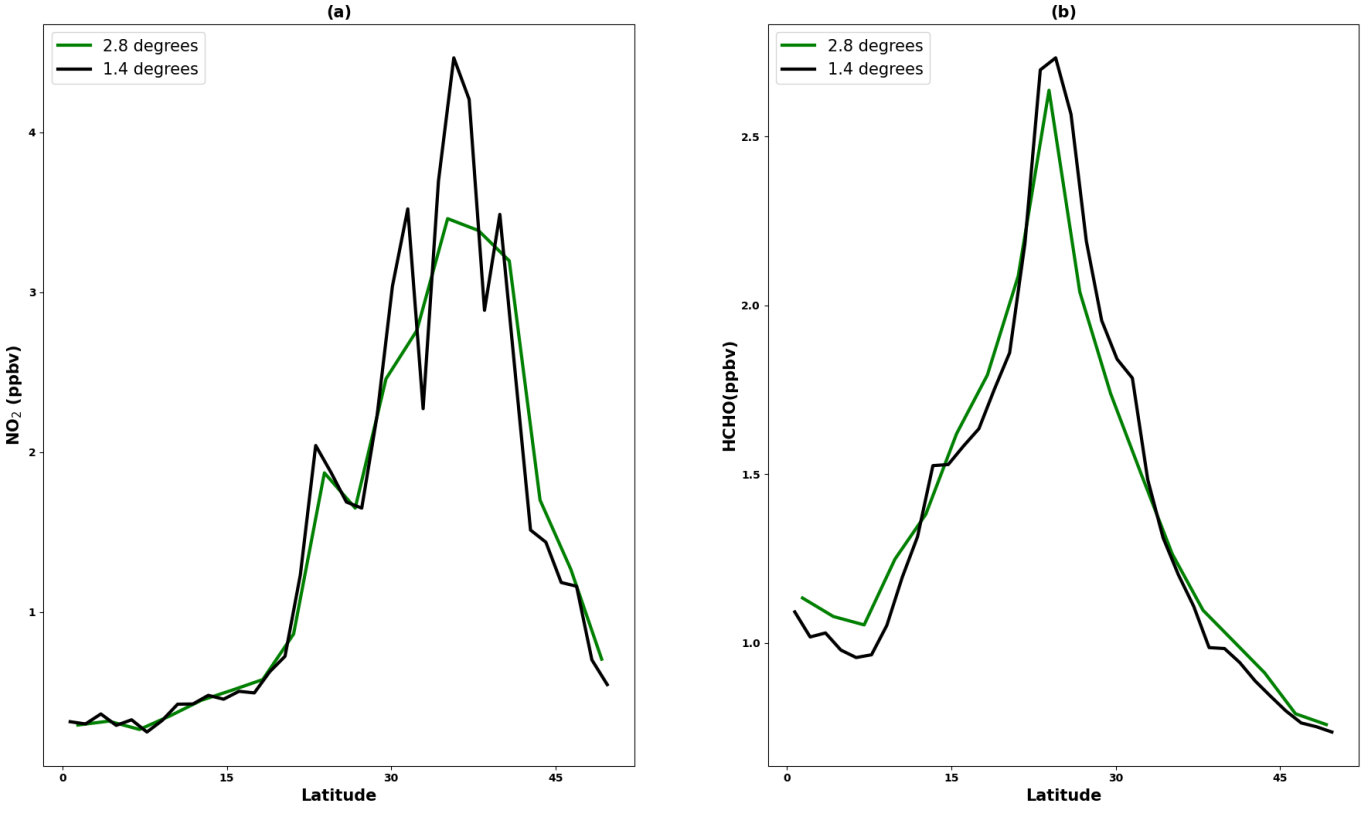

760

761

762 **Figure 12.** The zonal mean (a) NO_2, and (b) HCHO concentrations were estimated from CHASER simulations at
763 the spatial resolution of 2.8˚ ×2.8˚ (green) and 1.4˚ × 1.4˚(black). The latitude and longitude bound of the mean
764 values are 0˚-50˚N and 60˚ – 150˚E, respectively. The simulations for 2018 and daytime values from 09:00-
765 15:00 LT are plotted.

766

767 Chiba is not regarded as a major polluted region. Irie et al. (2021) reported a declining trend in NO_2 levels
768 in Chiba since 2012, echoing Miyazaki et al. (2020) 's results over Japan. The current model setting with
769 updated NO_x estimates would simulate a lower NO_2 level in Chiba than the observations. Therefore, the
770 impact of an updated emission inventories will also vary regionally. Data assimilation techniques can be
771 adopted to improve the model-observation comparison, which will be discussed in our future studies.

772

https://doi.org/10.5194/acp-2022-25
Preprint. Discussion started: 17 March 2022
© Author(s) 2022. CC BY 4.0 License.

Atmospheric Chemistry and Physics Discussions

773 ## 3.3 Contribution estimates

774 ### 3.3.1 Contribution from biomass burning to the HCHO and NO_2 abundances in Phimai

775 The good agreements between the datasets in the 0-1 km layer in Phimai can quantify biomass burning
776 contributions to the HCHO and NO_2 concentrations. Figure 13 presents the results of simulation
777 L1_HCHO, L1_opt, and L1_NO_2. The simulation settings are shown in Table 2. For better readability,
778 the switched-off emissions criterion is described in the legends of Fig. 13. The plots present the mean
779 concentrations in the 0–1 km layer. Biomass burning contributes ~10% to the HCHO concentrations in
780 Phimai during the dry season. However, based on the observations, a more substantial effect of biomass
781 burning is expected. During the wet season, the MAX-DOAS and CHASER HCHO concentrations are,
782 respectively, ~2 and ~4 ppbv, indicating overestimation of the biogenic emissions in CHASER. Figure
783 13(b) shows the HCHO concentration obtained from simulation L1_opt and MAX-DOAS observations
784 in 2017. In the L1_opt simulation setting, the biomass burning emissions are switched off; the biogenic
785 emissions are optimized to reproduce results analogous to those obtained from observations during the
786 wet season. In the absence of biomass burning, the surface HCHO concentrations in Phimai would be ~2
787 ppbv, resulting in a biomass burning contribution of ~20–50% during the dry season. The observed
788 interseason difference in the HCHO concentration in Phimai is ~60%. Consequently, the revised biomass
789 burning contribution estimate is more reasonable. Pyrogenic emissions contributions to the NO_2
790 concentrations in Phimai are ~10% during the dry season (Fig. 13(c)). Because the NO_2 concentrations
791 are low in Phimai, the simulation during March, when the influence of biomass burning is highest, is used
792 to derive a better contribution estimate. In the absence of biomass burning, the NO_2 concentration during
793 March would be ~0.84 ppbv (Fig.13(d)), indicating a contribution up to 35% to the NO_2 concentrations
794 in Phimai.

https://doi.org/10.5194/acp-2022-25
Preprint. Discussion started: 17 March 2022
© Author(s) 2022. CC BY 4.0 License.

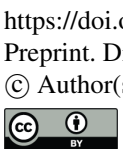

Atmospheric Chemistry and Physics Discussions

795

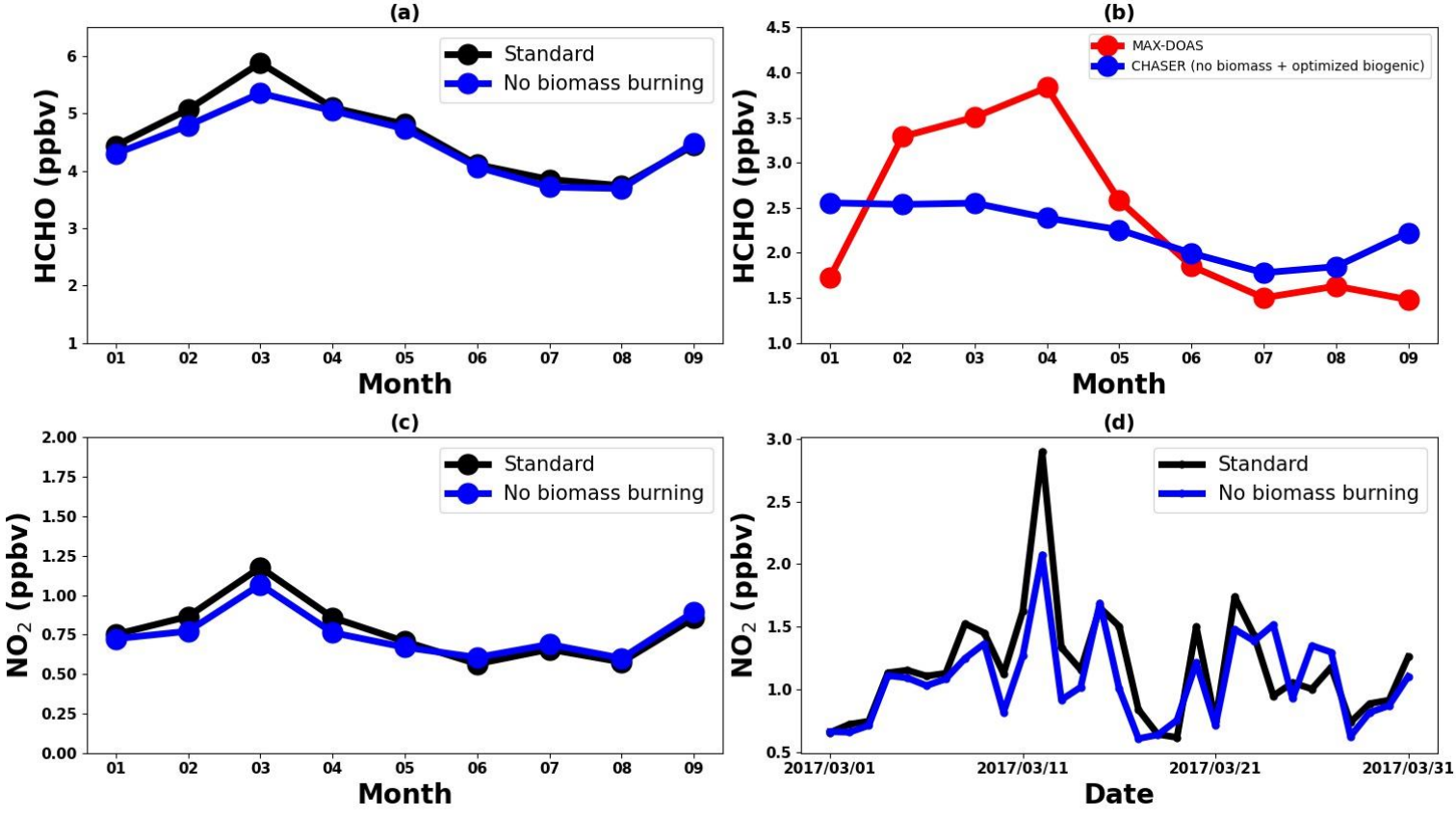

796

797 **Figure 13.** (top panel) The seasonal variations in the HCHO concentrations in the 0-1 km layer in Phimai, obtained
798 from the standard and L1_HCHO simulations. The pyrogenic emissions of VOCs are switched off in L1_HCHO.
799 (b) The HCHO seasonal variability in Phimai in 2017, obtained from the MAX-DOAS observations (red) and
800 L1_opt simulations. The pyrogenic VOC emissions were switched off, and the biogenic emissions were reduced
801 by 50% in L1_opt. The coincident dates between the observation and the simulations are plotted only. (bottom
802 panel) (c) The seasonal variations in the NO_2 surface concentrations in Phimai in 2017, obtained from the standard
803 and L1_NO_2 simulations. (d) Standard and L1_NO_2 simulation outputs of the daily mean NO_2 surface
804 concentrations during March 2017. The pyrogenic NO_2 emissions were switched off in the L1_NO_2 simulation.
805 Only the daytime values from 09:00 – 15:00 LT are used to calculate the seasonal mean.

806

807

https://doi.org/10.5194/acp-2022-25
Preprint. Discussion started: 17 March 2022
© Author(s) 2022. CC BY 4.0 License.

Atmospheric Chemistry and Physics Discussions

808 **3.3.2 Contribution of soil NOx emissions in Phimai**

809 Because soil NO_x emissions are included in CHASER simulations, the NO_2 contributions from soil
810 emissions ate quantified. Figure 14 presents the monthly mean surface NO_2 concentrations in Phimai in
811 2017, simulated including (standard) and switching off (L1_NO_2) the soil NO_x emissions. The NO_2
812 concentrations between 09 and 12 hr. were used to calculate the monthly mean concentrations. Soil
813 emissions contribute ~20% of the overall NO_2 concentrations in Phimai, with higher contributions during
814 the wet season. The highest soil contribution of about 25% occurs in July.

815

816 **3.3.3 Contribution from pyrogenic and anthropogenic emissions to the HCHO abundances in the**
817 **IGP region**

818 Figure 14(b) presents the standard, L1_HCHO (pyrogenic VOC emissions switched off), and L2
819 (anthropogenic VOC emissions switched off) HCHO simulations in the IGP region. According to
820 L1_HCHO simulation results, the effect of biomass burning emissions on the regional HCHO modulation
821 is small (~12%). The HCHO concentrations in India have biogenic, anthropogenic, and pyrogenic VOC
822 sources. However, Biogenic VOCs are the primary driver of the over HCHO variation (Surl et al., 2018).
823 Consequently, two potential reasons might be responsible for the small effects of pyrogenic emissions on
824 HCHO concentrations: (1) Overestimation of the biogenic emission or underestimation of pyrogenic
825 emissions in the model. (2) Stronger effects of anthropogenic VOC emissions than pyrogenic VOCs. The
826 L2 simulations show that anthropogenic emissions contribute up to 30% of the HCHO concentration in
827 the IGP region, with a maximum contributed during the post-monsoon season, which coincides with the
828 lower isoprene concentration (i.e., biogenic emissions) and temperature (Fig. 12(c)). Moreover, Kumar
829 and Sinha (2021) reported high acetaldehyde concentrations from anthropogenic emissions in the IGP
830 region throughout the year. Thus, anthropogenic emissions are likely to be a significant driver of HCHO
831 concentrations in the IGP region after biogenic emissions.

832

https://doi.org/10.5194/acp-2022-25
Preprint. Discussion started: 17 March 2022
© Author(s) 2022. CC BY 4.0 License.

Atmospheric Chemistry and Physics Discussions

833

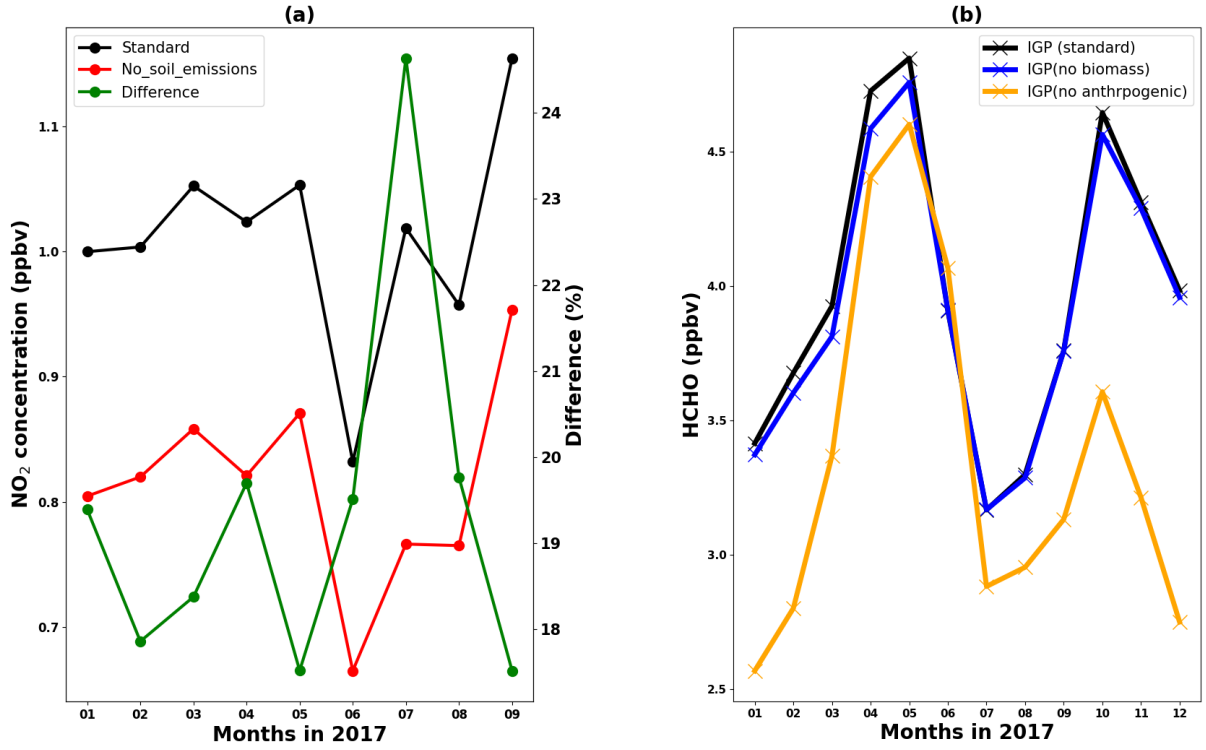

834

835 **Figure 14.** (a)The monthly mean NO_2 concentrations in Phimai were estimated from the standard (black) and
836 L1_NO_2 (red) simulations. The soil NO_x emissions are switched off in the LI_NO_2 simulation. The green line
837 indicates the percentage difference between the two simulations. (b) The seasonal variations in the HCHO
838 concentrations in the IGP region, obtained from the standard, L1_HCHO (pyrogenic VOC emission switched off),
839 and L2 simulations (anthropogenic VOC emissions switched off). The simulations for 2017 are plotted and
840 analyzed. Daytime values from 09:00-12:00 and 09:00 – 15:00 LT were selected for Phimai and IGP, respectively.

841

842

843

844

845

https://doi.org/10.5194/acp-2022-25
Preprint. Discussion started: 17 March 2022
© Author(s) 2022. CC BY 4.0 License.

Atmospheric Chemistry and Physics Discussions

4 Conclusions

NO_2 and HCHO concentrations and profiles are retrieved from MAX-DOAS observations at three A-SKY sites from January 2017 through December 2018, using the JM2 algorithm. The retrieved products were used to evaluate the global chemistry transport model CHASER simulations at the three sites. At all three locations, the seasonal variation of both trace gases was consistent throughout the investigated period. At Phimai and Pantnagar, biomass burning led to enhanced HCHO and NO_2 concentrations, respectively, during the dry season and spring and post-monsoon season. At Chiba, the HCHO variability was consistent with the temperature-led seasonal changes in the biogenic emissions. The changes in the dry season HCHO and NO_2 levels in Phimai from 2015 to 2018 were consistent with the number of fire events.

The R_{FN} values were biased towards a particular regime when the standard transition range $1 < R_{FN} < 2$ was used. The parameterization of Souri et al. (2020) provides a better estimate of the transition region. The classification results of the revised transition region in Phimai and Pantnagar contradicted the results based on the standard transition range; however, they were more reasonable. Such a method is based on observations, thus influenced by measurement constraints. More observational evidences are required to standardize this method. Overall, the results clarified that the standard transition region is not valid globally.

CHASER showed good skills in Phimai, characterized as a VOC-rich and low NO_2 (<1 ppbv) region. In both seasons, the observed and modeled profiles (HCHO and NO_2) agreed within the one sigma standard deviation of the measurements, despite a general overestimation of the model. Furthermore, both the wet season HCHO profiles were almost identical in the 0.5 – 4 km layer in both datasets.

At Pantnagar, the data within the 1.8 – 2 km layer were evaluated due to the mountainous terrain of the site. The simulated NO_2 concentrations around 2 km were less than 1 ppbv, moderately correlated with the observations with a maximum absolute difference ~0.2 ppbv. The model overestimated the HCHO level at the same height.

CHASER demonstrated limited performances in Chiba.NO_2 at higher resolution (i.e., 1.4˚) mainly improved the surface estimates, reducing the overall MBE in the 0-2 km layer by 35%. The finer

https://doi.org/10.5194/acp-2022-25
Preprint. Discussion started: 17 March 2022
© Author(s) 2022. CC BY 4.0 License.

Atmospheric Chemistry and Physics Discussions

resolution would improve the HCHO estimates in Chiba by 10%; however, it is yet to be underestimated. Sensitivity studies for the Phimai site estimated biomass burning contributions to the HCHO and NO_2 concentrations up to ~50 and ~ 35%, respectively. On average, 20% of the NO_2 level originates from soil NO_x emissions, which increased to 25% in July. Anthropogenic emissions (contribution up to 30%) have a more substantial impact on the VOC variability in the IGP region than biomass burning, consistent with reports in the literature.

Code availability. The CHASER and JM2 source codes are not available publicly. Dr. Kengo Sudo (kengo@nagoya-u.jp) is the contact person for readers and researchers interested in the CHASER model. In addition, Dr. Hitoshi Irie (hitoshi.irie@chiba-u.jp) will answer queries regarding the usage of the JM2 codes.

Data availability: The MAX-DOAS data used in the study are publicly accessible on the A-SKY network website (http://atmos3.cr.chiba-u.jp/a-sky/data.html). Upon request, the corresponding author can provide the CHASER simulations and MAX-DOAS averaging kernel data.

Author contributions: HMSH conceptualized the study, conducted the model simulations, analyzed the data, and drafted the manuscript. AMF helped with the data processing. HI developed the JM2 code and maintained the A-SKY network. KS developed the CHASER model and supervised the study. MN is the PI of the Pantnagar site. AD and MN shared their experience to explain the results. HI, KS, AD, MN, and AMF commented and provided feedback on the final results and manuscript.

Conflict of Interest: The authors declare that they have no conflict of Interest

Acknowledgments: This research is supported by the Global Environmental Research fund (S-12 and S-20) of the Ministry of the Environment (MOE), Japan, and JSPS KAKENHI Grants: JP20H04320, JP19HO5669, and JP19H04235. The CHASER model simulations are partly performed with the

https://doi.org/10.5194/acp-2022-25
Preprint. Discussion started: 17 March 2022
© Author(s) 2022. CC BY 4.0 License.

Atmospheric Chemistry and Physics Discussions

supercomputer (NEC SX-Aurora TSUBASA) at the National Institute for environmental studies (NIES), Tsukuba, Japan.

References

Arlander, D., Brüning, D., Schmidt, U., and Ehhalt, D. : The tropospheric distribution of formaldehyde during TROPOZ II, J. Atmos. Chem., 22(3), 251-269, https://doi.org/10.1007/BF00696637, 1995

Biswas, M. S., Ghude, S. D., Gurnale, D., Prabhakaran, T., and Mahajan, A. S. : Simultaneous Observations of Nitrogen Dioxide, Formaldehyde and Ozone in the Indo-Gangetic Plain. Aerosol Air Qual. Res., 19(8), 1749-1764, https://doi.org/10.4209/aaqr.2018.12.0484, 2019

Boeke, N. L., Marshall, J. D., Alvarez, S., Chance, K. V., Fried, A., Kurosu, T. P., Rappengluck, B., Richter, D.,Walega, J., & Weibring, P. (2011), Formaldehyde columns from the Ozone Monitoring Instrument: Urban versus background levels and evaluation using aircraft data and a global model. *J.Geophys.Res*, *116*(D5).

Bond, D. W., Zhang, R., Tie, X., Brasseur, G., Huffines, G., Orville, R. E., and Boccippio, D. J. : NO_x production by lightning over the continental United States, J. Geophys. Res., 106(D21), 27701-27710, https://doi.org/10.1029/2000JD000191, 2001

Bogumil, K., J. Orphal, T. Homann, S. Voigt, P. Spietz, O. Fleischmann, A. Vogel, M. Hartmann, H. Kromminga, and H. Bovensmann : Measurements of molecular absorption spectra with the SCIAMACHY pre-flight model: instrument characterization and reference data for atmospheric remote-sensing in the 230–2380 nm region, J. Photocho. Photobio. A, 157(2), 167-184, doi:10.1016/S1010-6030(03)00062-5, 2003

© Author(s) 2022. CC BY 4.0 License.

Burkert, J., Andrés-Hernández, M. D., Stöbener, D., Burrows, J. P., Weissenmayer, M., & Kraus, A. (2001) : Peroxy radical and related trace gas measurements in the boundary layer above the Atlantic Ocean, J. Geophys. Res., 106(D6), 5457-5477, https://doi.org/10.1029/2000JD900613, 2001

Cárdenas, L., Rondón, A., Johansson, C., & Sanhueza, E. : Effects of soil moisture, temperature, and inorganic nitrogen on nitric oxide emissions from acidic tropical savannah soils. J. Geophys. Res., 98(D8), 14783-14790, https://doi.org/10.1029/93JD01020, 1993

Chaliyakunnel, S., Millet, D. B., and Chen, X. : Constraining emissions of volatile organic compounds over the Indian subcontinent using space-based formaldehyde measurements. J. Geophys. Res., 124(19), 10525-10545, https://doi.org/10.1029/2019JD031262, 2019

Chance, K. V., and R. J. D. Spurr. : Ring effect studies: Rayleigh scattering, including molecular parameters for rotational Raman scattering: and the Fraunhofer spectrum, *Appl. Opt.* , *36*(21), 5224-5230 doi:10.1364/AO.36.005224,1997

Clémer, K., Van Roozendael, M., Fayt, C., Hendrick, F., Hermans, C., Pinardi, G., Spurr, R., Wang, P., and De Mazière, M. : Multiple wavelength retrieval of tropospheric aerosol optical properties from MAXDOAS measurements in Beijing, Atmos. Meas. Tech., 3(4), 863-878, https://doi.org/10.5194/amt-3-863-2010, 2010

© Author(s) 2022. CC BY 4.0 License.


Colella, P., & Woodward, P. R. : The piecewise parabolic method (PPM) for gas-dynamical simulations. J. Comput. Phys., 54(1), 174-201, https://doi.org/10.1016/0021-9991(84)90143-8, 1984

Crutzen, P. J. : The influence of nitrogen oxides on the atmospheric ozone content. Q. J. Roy. Meteor. Soc., 96(408), 320-325, https://doi.org/10.1002/qj.49709640815, 1970

Davidson, E. A., Vitousek, P. M., Matson, P. A., Riley, R., García-Méndez, G., & Maass, J. M. : Soil emissions of nitric oxide in a seasonally dry tropical forest of Mexico. *J. Geophys. Res.*, *96*(D8), 15439-15445, https://doi.org/10.1029/91JD01476, 1991

Duncan, B. N., Yoshida, Y., Damon, M. R., Douglass, A. R., and Witte, J. C. : Temperature dependence of factors controlling isoprene emissions. Geophys. Res. Lett., 36(5), https://doi.org/10.1029/2008GL037090, 2009

Emori, S., Nozawa, T., Numaguti, A., & Uno, I. : Importance of cumulus parameterization for precipitation simulation over East Asia in June. J. Meteorol. Soc. Jpn., 79(4), 939-947. https://doi.org/10.2151/jmsj.79.939, 2001

© Author(s) 2022. CC BY 4.0 License.


Fleischmann, O. C., M. Hartmann, J. P. Burrows, and J. Orphal : New ultraviolet absorption cross-sections of BrO at atmospheric temperatures measured by time-windowing Fourier transform spectroscopy, *J. Photocho. Photobio. A*, *168*(1), 117-132, doi:10.1016/j.jphotochem.2004.03.026, 2004

Franco, B., Hendrick, F., Van Roozendael, M., Müller, J.-F., Stavrakou, T., Marais, E. A., Bovy, B., Bader, W., Fayt, C., Hermans, C., Lejuene, B., Pinardi, G., Sevais, C., and Mahieu, E. : Retrievals of formaldehyde from ground-based FTIR and MAX-DOAS observations at the Jungfraujoch station and comparisons with GEOS-Chem and IMAGES model simulations. Atmos. Meas. Tech., 8(4), 1733-1756, https://doi.org/10.5194/amt-8-1733-2015, 2015

Fu, T. M., Jacob, D. J., Wittrock, F., Burrows, J. P., Vrekoussis, M., and Henze, D. K. : Global budgets of atmospheric glyoxal and methylglyoxal, and implications for formation of secondary organic aerosols, J. Geophys. Res., 113(D15), https://doi.org/10.1029/2007JD009505, 2008

Frieß, U., Monks, P. S., Remedios, J. J., Rozanov, A., Sinreich, R., Wagner, T., & Platt, U. : MAX-DOAS O4 measurements: A new technique to derive information on atmospheric aerosols: 2. Modeling studies. J. Geophys. Res., 111(D14), https://doi.org/10.1029/2005JD006618, 2006

Frieß, U., Klein Baltink, H., Beirle, S., Clémer, K., Hendrick, F., Henzing, B., Irie, H., de Leeuw, G., Li, A., Moerman, M. M., van Roozendael, M., Shaiganfar, R., Wagner, T., Wang, Y., Xie, P., Yilmaz, S., and Zieger, P. : Intercomparison of aerosol extinction profiles retrieved from MAX-DOAS measurements. Atmos. Meas.Tech., 9(7), 3205-3222, https://doi.org/10.5194/amt-9-3205-2016, 2016

© Author(s) 2022. CC BY 4.0 License.


Hak, C., Pundt, I., Trick, S., Kern, C., Platt, U., Dommen, J., Ordóñez, C., Prévôt, A. S. H., Junkermann, W., Astorga-Lloréns, C., Larsen, B. R., Mellqvist, J., Strandberg, A., Yu, Y., Galle, B., Kleffmann, J., Lörzer, J. C., Braathen, G. O., and Volkamer, R. : Intercomparison of four different in-situ techniques for ambient formaldehyde measurements in urban air, *Atmos. Chem. Phys.*, *5*(11), 2881-2900. https://doi.org/10.5194/acp-5-2881-2005, 2005

Hall, S. J., Matson, P. A., and Roth, P. M. : NO_x emissions from soil: implications for air quality modeling in agricultural regions. Annu. Rev. Energy Environ., 21(1), 311-346. https://doi.org/10.1146/annurev.energy.21.1.311, 1996

Halla, J. D., Wagner, T., Beirle, S., Brook, J. R., Hayden, K. L., O'Brien, J. M., Ng, A., Majonis, D., Wenig, M. O., and McLaren, R : Determination of tropospheric vertical columns of NO 2 and aerosol optical properties in a rural setting using MAX-DOAS. Atmos. Chem. Phys., 11(23), 12475-12498, https://doi.org/10.5194/acp-11-12475-2011, 2011

Hendrick, F., Müller, J.-F., Clémer, K., Wang, P., De Mazière, M., Fayt, C., Gielen, C., Hermans, C., Ma, J. Z., Pinardi, G., Stavrakou, T., Vlemmix, T., and Van Roozendael, M.: Four years of ground-based MAX-DOAS observations of HONO and NO_2 in the Beijing area, Atmos. Chem. Phys., 14(2), 765-781, https://doi.org/10.5194/acp-14-765-2014, 2014

Hermans, C., A. Vandaele, S. Fally, M. Carleer, R. Colin, B. Coquart, A. Jenouvrier, and M.-F. Merienne. : Absorption cross-section of the collision-induced bands of oxygen from the UV to the NIR, in Weakly interacting molecular pairs: unconventional absorbers of radiation in the atmosphere, edited, pp. 193-202, Springer,2003.

© Author(s) 2022. CC BY 4.0 License.

Hönninger, G., Friedeburg, C. v., and Platt, U. : Multi axis differential optical absorption spectroscopy (MAX-DOAS), Atmos. Chem. Phys., 4(1), 231-254, https://doi.org/10.5194/acp-4-231-2004, 2004

Hoque, H.M. S., Irie, H., and Damiani, A. (2018). First MAX-DOAS Observations of Formaldehyde and Glyoxal in Phimai, Thailand. J. Geophys. Res., 123(17), 9957-9975, https://doi.org/10.1029/2018JD028480, 2018a

Hoque, H. M. S., Irie, H., Damiani, A., Rawat, P., and Naja, M. : First simultaneous observations of formaldehyde and glyoxal by MAX-DOAS in the Indo-Gangetic Plain region. *Sola*. , https://doi.org/10.2151/sola.2018-028, 2018b

Houweling, S., Dentener, F., and Lelieveld, J. : The impact of nonmethane hydrocarbon compounds on tropospheric photochemistry. J. Geophys. Res., 103(D9), 10673-10696, https://doi.org/10.1029/97JD03582, 1998

Huber, D. E., Steiner, A. L., & Kort, E. A. : Daily Cropland Soil NO_x Emissions Identified by TROPOMI and SMAP. Geophys. Res. Lett., 47(22), e2020GL089949, https://doi.org/10.1029/2020GL089949, 2020

Irie, H., Kanaya, Y., Akimoto, H., Iwabuchi, H., Shimizu, A., & Aoki, K. : First retrieval of tropospheric aerosol profiles using MAX-DOAS and comparison with lidar and sky radiometer measurements. Atmos. Chem. Phys., 8(2), 341-350, https://doi.org/10.5194/acp-8-341-2008, 2008a

Irie, H., Kanaya, Y., Akimoto, H., Tanimoto, H., Wang, Z., Gleason, J. F., & Bucsela, E. J. : Validation of OMI tropospheric NO_2 column data using MAX-DOAS measurements deep inside the North China Plain in June 2006: Mount Tai Experiment 2006. Atmos. Chem. Phys., 8(22), 6577-6586,https://doi.org/10.5194/acp-8-6577-2008, 2008b.

© Author(s) 2022. CC BY 4.0 License.


Irie, H., Kanaya, Y., Akimoto, H., Iwabuchi, H., Shimizu, A., & Aoki, K. : Dual-wavelength aerosol vertical profile measurements by MAX-DOAS at Tsukuba, Japan. *Atmos. Chem. Phys.*, *9*(8), 2741-2749, https://doi.org/10.5194/acp-9-2741-2009, 2009

Irie, H., Takashima, H., Kanaya, Y., Boersma, K., Gast, L., Wittrock, F., Brunner, D., Zhou, Y., Roozendael, M. V. : Eight-component retrievals from ground-based MAX-DOAS observations. Atmos. Meas. Tech., 4(6), 1027-1044, https://doi.org/10.5194/amt-4-1027-2011, 2011

Irie, H., Nakayama, T., Shimizu, A., Yamazaki, A., Nagai, T., Uchiyama, A., Zaizen, Y., Kagamitani, S., and Matsumi, Y. : Evaluation of MAX-DOAS aerosol retrievals by coincident observations using CRDS, lidar, and sky radiometer inTsukuba, Japan. Atmos. Meas.Tech., 8(7), 2775-2788, https://doi.org/10.5194/amt-8-2775-2015, 2015

Ito, A., and Inatomi, M. : Use of a process-based model for assessing the methane budgets of global terrestrial ecosystems and evaluation of uncertainty. Biogeosciences, 9(2), 759-773. https://doi.org/10.5194/bg-9-759-2012, 2012

Iwabuchi, H. :Efficient Monte Carlo methods for radiative transfer modeling. J. Atmos. Sci., 63(9), 2324-2339, https://doi.org/10.1175/JAS3755.1, 2006

Jang, M., and Kamens, R. M. : Characterization of secondary aerosol from the photooxidation of toluene in the presence of NO_x and 1-propene, Environ. Sci. Technol., 35(18), 3626-3639. https://doi.org/10.1021/es010676+, 2001

Jin, X., Fiore, A. M., Murray, L. T., Valin, L. C., Lamsal, L. N., Duncan, B., Boersma, K.F., De Smedt, I., Abad, G.G., Chance, K., and Tonnesen, G. : Evaluating a space-based indicator of surface ozone-NOx-VOC

© Author(s) 2022. CC BY 4.0 License.

sensitivity over midlatitude source regions and application to decadal trends. J. Geophys. Res., 122(19), 10,439-410,461, https://doi.org/10.1002/2017JD026720, 2017

Jin, X., & Holloway, T. (2015). Spatial and temporal variability of ozone sensitivity over China observed from the Ozone Monitoring Instrument. J. Geophys.Res., 120(14), 7229-7246. doi: https://doi.org/10.1002/2015JD023250

K-1 model developers : K-1 Coupled GCM (MIROC) description, Tech .rep., Center for Climate System Research (University of Tokyo), National Institute for Environemntal Studies, and Frontier Research Center for Global Change, available at : http://ccsr.aori.u-tokyo.ac.jp/~hasumi/miroc_description.pdf, 2004

Kanakidou, M., Seinfeld, J. H., Pandis, S. N., Barnes, I., Dentener, F. J., Facchini, M. C., Van Dingenen, R., Ervens, B., Nenes, A., Nielsen, C. J., Swietlicki, E., Putaud, J. P., Balkanski, Y., Fuzzi, S., Horth, J., Moortgat, G. K., Winterhalter, R., Myhre, C. E. L., Tsigaridis, K., Vignati, E., Stephanou, E. G., and Wilson, J. : Organic aerosol and global climate modelling: a review. Atmos. Chem. Phys., 5(4), 1053-1123, https://doi.org/10.5194/acp-5-1053-2005

Kanaya, Y., Irie, H., Takashima, H., Iwabuchi, H., Akimoto, H., Sudo, K., Gu, M., Chong, J., Kim, Y. J., Lee, H., Li, A., Si, F., Xu, J., Xie, P.-H., Liu, W.-Q., Dzhola, A., Postylyakov, O., Ivanov, V., Grechko, E., Terpugova, S., and Panchenko, M.: Long-term MAX-DOAS network observations of NO₂ in Russia and Asia (MADRAS) during the period 2007–2012: instrumentation, elucidation of climatology, and comparisons with OMI satellite observations and global model simulations. Atmos. Chem. Phys., 14(15), 7909-7927, https://doi.org/10.5194/acp-14-7909-2014, 2014

Kreher, K., Van Roozendael, M., Hendrick, F., Apituley, A., Dimitropoulou, E., Frieß, U., Richter, A., Wagner, T., Lampel, J., Abuhassan, N., Ang, L., Anguas, M., Bais, A., Benavent, N., Bösch, T., Bognar, K.,

© Author(s) 2022. CC BY 4.0 License.

Borovski, A., Bruchkouski, I., Cede, A., Chan, K. L., Donner, S., Drosoglou, T., Fayt, C., Finkenzeller, H., Garcia-Nieto, D., Gielen, C., Gómez-Martín, L., Hao, N., Henzing, B., Herman, J. R., Hermans, C., Hoque, S., Irie, H., Jin, J., Johnston, P., Khayyam Butt, J., Khokhar, F., Koenig, T. K., Kuhn, J., Kumar, V., Liu, C., Ma, J., Merlaud, A., Mishra, A. K., Müller, M., Navarro-Comas, M., Ostendorf, M., Pazmino, A., Peters, E., Pinardi, G., Pinharanda, M., Piters, A., Platt, U., Postylyakov, O., Prados-Roman, C., Puentedura, O., Querel, R., Saiz-Lopez, A., Schönhardt, A., Schreier, S. F., Seyler, A., Sinha, V., Spinei, E., Strong, K., Tack, F., Tian, X., Tiefengraber, M., Tirpitz, J.-L., van Gent, J., Volkamer, R., Vrekoussis, M., Wang, S., Wang, Z., Wenig, M., Wittrock, F., Xie, P. H., Xu, J., Yela, M., Zhang, C., and Zhao, X.: Intercomparison of NO_2, O_4, O_3 and HCHO slant column measurements by MAX-DOAS and zenith-sky UV–visible spectrometers during CINDI-2. Atmos. Meas. Tech., 13(5), 2169-2208, https://doi.org/10.5194/amt-13-2169-2020, 2020

Kumar, V., Beirle, S., Dörner, S., Mishra, A. K., Donner, S., Wang, Y., Sinha,V., and Wagner, T. (2020). Long-term MAX-DOAS measurements of NO2, HCHO, and aerosols and evaluation of corresponding satellite data products over Mohali in the Indo-Gangetic Plain. Atmos. Chem. Phys., *20*(22), 14183-14235. doi:10.5194/acp-20-14183-2020

Kumar, V., & Sinha, V. (2021), Season-wise analyses of VOCs, hydroxyl radicals and ozone formation chemistry over north-west India reveal isoprene and acetaldehyde as the most potent ozone precursors throughout the year. Chemosphere, *283*, 131184. doi:https://doi.org/10.1016/j.chemosphere.2021.131184

Kurucz, R. L., Furenlid, I., Brault, J., and Testerman, L. : Solar Flux Atlas from 296 to 1300 nm. Natl. Sol. Obs., Sunspot, New Mexico, 240, 1984

Lee, M., Heikes, B. G., Jacob, D. J., Sachse, G., and Anderson, B. : Hydrogen peroxide, organic hydroperoxide, and formaldehyde as primary pollutants from biomass burning, J. Geophys. Res., 102(D1), 1301-1309, https://doi.org/10.1029/96JD01709, 1997

© Author(s) 2022. CC BY 4.0 License.


Lin, S.-J., & Rood, R. B. : Multidimensional flux-form semi-Lagrangian transport schemes. Mon. Weather Rev., 124(9), 2046-2070, https://doi.org/10.1175/1520-0493(1996)124<2046:MFFSLT>2.0.CO;2, 1996

Ma, J., Beirle, S., Jin, J., Shaiganfar, R., Yan, P., and Wagner, T. : Tropospheric NO_2 vertical column densities over Beijing: results of the first three years of ground-based MAX-DOAS measurements (2008–2011) and satellite validation,Atmos. Chem. Phys., 13(3), 1547-1567, https://doi.org/10.5194/acp-13-1547-2013, 2013

Mallik, C., & Lal, S. : Seasonal characteristics of SO_2, NO_2, and CO emissions in and around the Indo-Gangetic Plain, Environ Monit Assess, *186*(2), 1295-1310, https://doi.org/10.1007/s10661-013-3458-y,2015

Martin, R. V., Fiore, A. M., and Van Donkelaar, A. : Space-based diagnosis of surface ozone sensitivity to anthropogenic emissions, Geophys. Res. Lett., 31(6), https://doi.org/10.1029/2004GL019416, 2004

Mahajan, A. S., De Smedt, I., Biswas, M. S., Ghude, S., Fadnavis, S., Roy, C., and van Roozendael, M. : Inter-annual variations in satellite observations of nitrogen dioxide and formaldehyde over India. Atmos. Environ., 116, 194-201, https://doi.org/10.1016/j.atmosenv.2015.06.004, 2015

© Author(s) 2022. CC BY 4.0 License.

Meller, R., and G. K. Moortgat. : Temperature dependence of the absorption cross sections of formaldehyde between 223 and 323 K in the wavelength range 225–375 nm, *J. Geophys. Res.*, *105*(D6), 7089-7101, doi:10.1029/1999JD901074, 2000

Mellor, G. L., & Yamada, T. : A hierarchy of turbulence closure models for planetary boundary layers. J. Atmos. Sci., 31(7), 1791-1806, https://doi.org/10.1175/1520-0469(1974)031<1791:AHOTCM>2.0.CO;2, 1974

Mishra, A. K., and Sinha, V. : Emission drivers and variability of ambient isoprene, formaldehyde and acetaldehyde in north-west India during monsoon season, Environ. Pollut., 267, 115538, https://doi.org/10.1016/j.envpol.2020.115538, 2020

Miyazaki, K., Bowman, K., Sekiya, T., Eskes, H., Boersma, F., Worden, H., Livesey, N., Payne, V.H., Sudo, K., Kanaya, Y., Takigawa, M., and Ogochi, K. (2020). Updated tropospheric chemistry reanalysis and emission estimates, TCR-2, for 2005–2018. Earth Syst. Sci. Data, 12(3), 2223-2259. doi:10.5194/essd-12-2223-2020

Miyazaki, K., Eskes, H., Sudo, K., Boersma, K. F., Bowman, K., and Kanaya, Y. : Decadal changes in global surface NOx emissions from multi-constituent satellite data assimilation. Atmos. Chem. Phys., 17(2), 807-837, https://doi.org/10.5194/acp-17-807-2017, 2017

Platt, U. : Differential optical absorption spectroscopy (DOAS), in Chemical Analysis Series, edited, pp. 27-84, Wiley & Sons. Inc., 1994

Platt, U., and Stutz, J. : Differential Optical Absorption Spectroscopy, Springer, 2008

© Author(s) 2022. CC BY 4.0 License.


Price, C., & Rind, D. : A simple lightning parameterization for calculating global lightning distributions. *J. Geophys. Res.*, *97*(D9), 9919-9933, https://doi.org/10.1029/92JD00719, 1992

Rodgers, C. D. : Inverse methods for atmospheric sounding: theory and practice, World scientific Singapore, 2008

Roscoe, H. K., Van Roozendael, M., Fayt, C., du Piesanie, A., Abuhassan, N., Adams, C., Akrami, M., Cede, A., Chong, J., Clémer, K., Friess, U., Gil Ojeda, M., Goutail, F., Graves, R., Griesfeller, A., Grossmann, K., Hemerijckx, G., Hendrick, F., Herman, J., Hermans, C., Irie, H., Johnston, P. V., Kanaya, Y., Kreher, K., Leigh, R., Merlaud, A., Mount, G. H., Navarro, M., Oetjen, H., Pazmino, A., Perez-Camacho, M., Peters, E., Pinardi, G., Puentedura, O., Richter, A., Schönhardt, A., Shaiganfar, R., Spinei, E., Strong, K., Takashima, H., Vlemmix, T., Vrekoussis, M., Wagner, T., Wittrock, F., Yela, M., Yilmaz, S., Boersma, F., Hains, J., Kroon, M., Piters, A., and Kim, Y. J. : Intercomparison of slant column measurements of NO_2 and O_4 by MAX-DOAS and zenith-sky UV and visible spectrometers. Atmos. Meas. Tech., 3(6), 1629-1646, https://doi.org/10.5194/amt-3-1629-2010, 2010

Ryan, R. G., Rhodes, S., Tully, M., & Schofield, R. : Surface ozone exceedances in Melbourne, Australia are shown to be under NO_x control, as demonstrated using formaldehyde: NO_2 and glyoxal: formaldehyde ratios, Sci. Total Environ., 749, 141460, https://doi.org/10.1016/j.scitotenv.2020.141460, 2020

Schindlbacher, A., Zechmeister-Boltenstern, S., & Butterbach-Bahl, K. : Effects of soil moisture and temperature on NO, NO_2, and N_2O emissions from European forest soils. J. Geophys. Res., 109(D17), https://doi.org/10.1029/2004JD004590, 2004

Schroeder, J. R., Crawford, J. H., Fried, A., Walega, J., Weinheimer, A., Wisthaler, A., Muller, M., Mikovinu, T., Chen,G., Shook, M. : New insights into the column CH_2O/NO_2 ratio as an indicator of near-surface ozone sensitivity. J.Geophys. Res., 122(16), 8885-8907. doi: https://doi.org/10.1002/2017JD026781,2017

© Author(s) 2022. CC BY 4.0 License.

Seco, R., Penuelas, J., and Filella, I. : Short-chain oxygenated VOCs: Emission and uptake by plants and atmospheric sources, sinks, and concentrations, Atmos. Environ., 41(12), 2477-2499, https://doi.org/10.1016/j.atmosenv.2006.11.029, 2007

Sekiya, T., & Sudo, K. : Roles of transport and chemistry processes in global ozone change on interannual and multidecadal time scales. J. Geophys. Res., 119(8), 4903-4921. doi:https://doi.org/10.1002/2013JD020838, 2014

Sekiya, T., Miyazaki, K., Ogochi, K., Sudo, K., & Takigawa, M. : Global high-resolution simulations of tropospheric nitrogen dioxide using CHASER V4.0. *Geosci. Model Dev.*, *11*(3), 959-988. http://doi.org/10.5194/gmd-11-959-2018, 2018

Seinfeld, J. H., & Pandis, S. N. : Atmospheric chemistry and physics: from air pollution to climate change: John Wiley & Sons, New York, 1998

Singh, H., Salas, L., Chatfield, R., Czech, E., Fried, A., Walega, J., Evans, M.J., Field, B.D., Jacob, D.J., Blake, D., Heikes, B., Talbolt, R., Sachse, G., Crawford, J.H., Avery, M.A., Sandholm, S., and Fuelberg, H. : Analysis of the atmospheric distribution, sources, and sinks of oxygenated volatile organic chemicals based on measurements over the Pacific during TRACE-P, J. Geophys. Res., 109(D15), https://doi.org/10.1029/2003JD003883, 2004

Sinreich, R., Frieß, U., Wagner, T., and Platt, U. : Multi axis differential optical absorption spectroscopy (MAX-DOAS) of gas and aerosol distributions, Faraday discuss., 130, 153-164, https://doi.org/10.1039/B419274P, 2005

© Author(s) 2022. CC BY 4.0 License.

1302 Solomon, S., Portmann, R., Sanders, R., Daniel, J., Madsen, W., Bartram, B., and Dutton, E. : On the role of
1303 nitrogen dioxide in the absorption of solar radiation, J. Geophys. Res., 104(D10), 12047-12058,
1304 https://doi.org/10.1029/1999JD900035, 1999
1305
1306
1307 Souri, A. H., Nowlan, C. R., Wolfe, G. M., Lamsal, L. N., Miller, C. E. C., Abad, G. G., Janz, S., Fried, A., Blake,
1308 D. R., Weinheimer, A. J. , Diskin, G.S., Liu, X., and Chance, K. : Revisiting the effectiveness of
1309 HCHO/NO_2 ratios for inferring ozone sensitivity to its precursors using high resolution airborne remote
1310 sensing observations in a high ozone episode during the KORUS-AQ campaign. Atmos. Environ., 224,
1311 117341, https://doi.org/10.1016/j.atmosenv.2020.117341, 2020
1312
1313
1314 Sudo, K., & Akimoto, H. (2007). Global source attribution of tropospheric ozone: Long-range transport from
1315 various source regions. J. Geeophys. Res., 112(D12), https://doi.org/10.1029/2006JD007992, 2007
1316
1317 Sudo, K., Takahashi, M., Kurokawa, J., & Akimoto, H. : CHASER: A global chemical model of the troposphere
1318 1. Model description. J. Geophys. Res., 107, 4339, https://doi.org/10.1029/2001JD001113, 2002
1319
1320 Surl, L., Palmer, P. I., & González Abad, G. : Which processes drive observed variations of HCHO columns over
1321 India? Atmos. Chem. Phys., 18(7), 4549-4566 ,https://doi.org/10.5194/acp-18-4549-2018, 2018
1322
1323
1324 Takemura, T., Nozawa, T., Emori, S., Nakajima, T. Y., & Nakajima, T. : Simulation of climate response to aerosol
1325 direct and indirect effects with aerosol transport-radiation model. J. Geophys. Res., 110(D2),
1326 https://doi.org/10.1029/2004JD005029, 2005
1327
1328 Takemura, T., Egashira, M., Matsuzawa, K., Ichijo, H., O'ishi, R., & Abe-Ouchi, A. : A simulation of the global
1329 distribution and radiative forcing of soil dust aerosols at the Last Glacial Maximum. Atmos. Chem. Phys.,
1330 9(9), 3061-3073, https://doi.org/10.5194/acp-9-3061-2009, 2009
1331

© Author(s) 2022. CC BY 4.0 License.

Tonnesen, G. S., & Dennis, R. L. (2000). Analysis of radical propagation efficiency to assess ozone sensitivity to hydrocarbons and NO_x: 1. Local indicators of instantaneous odd oxygen production sensitivity. J.Geophys. Res., 105(D7), 9213-9225. doi:https://doi.org/10.1029/1999JD900371

Vandaele, A., C. Hermans, P. Simon, M. Van Roozendael, J. Guilmot, M. Carleer, and R. Colin.: Fourier transform measurement of NO2 absorption cross-section section in the visible range at room temperature, J. Atmos. Chem., 25(3), 289-305, doi:10.1007/BF00053797, 2009

Vandaele, A. C., C. Fayt, F. Hendrick, C. Hermans, F. Humbled, M. V. Roozendael, M. Gil, M. Navarro, O. Puentedura, M. Yela, G. Braathen, K. Stebel, K. Tornkvist, P. Jhonston, K. Kreher, F. Goutail, F. Mieville, J.P. Pommereau, S. Khaikine, A. Richter, H. Oetjen, F. Wittrock, S. Bugarski, U. Friess, K. Pfeilsticker, R. Sinreich, T. Wagner, G. Corlett, and R. Leigh), An intercomparison campaign of ground-based UV-visible measurements of NO_2, BrO, and OClO slant columns Methods of analysis and results for NO_2, J. Geophys Res, 110(D8),2005

Vigouroux, C., Hendrick, F., Stavrakou, T., Dils, B., De Smedt, I., Hermans, C., Merlaud, A., Scolas, F., Senten, C., Vanhaelewyn, G., Fally, S., Carleer, M., Metzger, J.-M., Müller, J.-F., Van Roozendael, M., and De Mazière, M.: Ground-based FTIR and MAX-DOAS observations of formaldehyde at Réunion Island and comparisons with satellite and model data, Atmos. Chem. Phys., 9(24), 9523-9544, https://doi.org/10.5194/acp-9-9523-2009, 2009

Wagner, T., Dix, B. v., Friedeburg, C. v., Frieß, U., Sanghavi, S., Sinreich, R., & Platt, U. : MAX-DOAS O4 measurements: A new technique to derive information on atmospheric aerosols—Principles and information content. J. Geophys. Res., 109(D22). doi: https://doi.org/10.1029/2004JD004904, 2004

© Author(s) 2022. CC BY 4.0 License.

Wagner, T., Burrows, J., Deutschmann, T., Dix, B., Friedeburg, C. v., Frieß, U., Iwabuchi, H. , Hendrick, F., Heue, K.-P., Irie, H., Iwabuchi, H., Kanaya, Y., Keller, J., McLinden, C. A., Oetjen, H., Palazzi, E., Petritoli, A., Platt, U., Postylyakov, O., Pukite, J., Richter, A., van Roozendael, M., Rozanov, A., Rozanov, V., Sinreich, R., Sanghavi, S., and Wittrock, F. : Comparison of box-air-mass-factors and radiances for Multiple-Axis Differential Optical Absorption Spectroscopy (MAX-DOAS) geometries calculated from different UV/visible radiative transfer models. Atmos. Chem. Phys., 7(7), 1809-1833. doi:https://doi.org/10.5194/acp-7-1809-2007, 2007

Wang, T., Hendrick, F., Wang, P., Tang, G., Clémer, K., Yu, H., Fayt, C., Hermans, C., Gielen, C., Müller, J.-F., Pinardi, G., Theys, N., Brenot, H., and Van Roozendael, M. : Evaluation of tropospheric SO_2 retrieved from MAX-DOAS measurements in Xianghe, China. Atmos. Chem. Phys., 14(20), 11149-11164, https://doi.org/10.5194/acp-14-11149-2014, 2014

Wesely, M. : Parameterization of surface resistances to gaseous dry deposition in regional-scale numerical models. Atmos. Environ., 41, 52-63. https://doi.org/10.1016/j.atmosenv.2007.10.058, 1989

Williams, J. E., Boersma, K. F., Sager, P. L., & Verstraeten, W. W,. The high-resolution version of TM5-MP for optimized satellite retrievals: description and validation. Geosci. Model Dev., 10(2), 721-750. doi:https://doi.org/10.5194/gmd-10-721-2017,2017

Wittrock, F., Oetjen, H., Richter, A., Fietkau, S., Medeke, T., Rozanov, A., and Burrows, J. : MAX-DOAS measurements of atmospheric trace gases in Ny-Ålesund-Radiative transfer studies and their application, Atmos. Chem. Phys., 4(4), 955-966, https://doi.org/10.5194/acp-4-955-2004, 2004